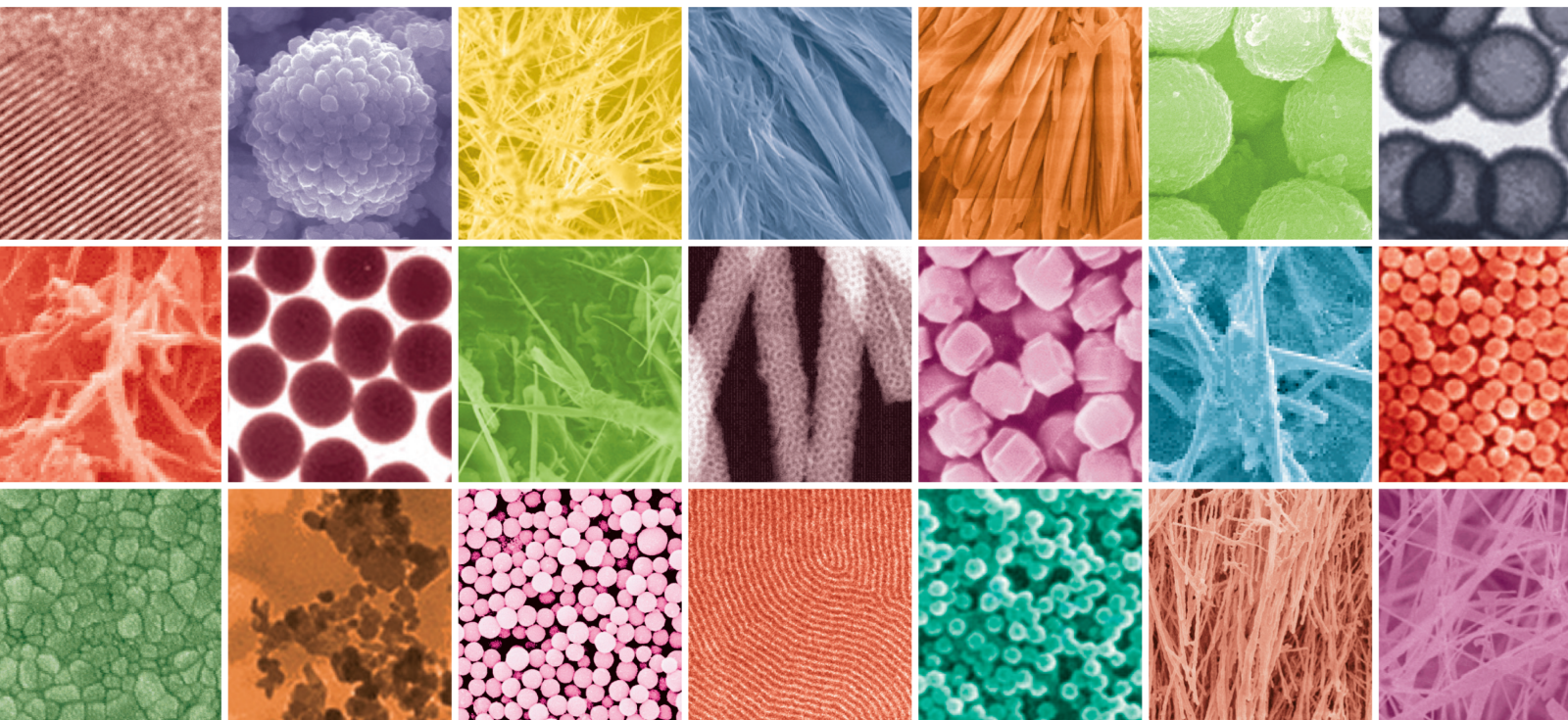


New Trends in Antimicrobial Nanostructures

Lead Guest Editor: Ahmad Gholami

Guest Editors: Navid Omidifar, Seyyed Alireza Hashemi, and Seyyed
mojtaba Mousavi





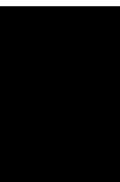
New Trends in Antimicrobial Nanostructures

Journal of Nanomaterials

New Trends in Antimicrobial Nanostructures

Lead Guest Editor: Ahmad Gholami

Guest Editors: Navid Omidifar, Seyyed Alireza Hashemi, and Seyyed mojtaba Mousavi






Copyright © 2022 Hindawi Limited. All rights reserved.

This is a special issue published in "Journal of Nanomaterials." All articles are open access articles distributed under the Creative Commons Attribution License, which permits unrestricted use, distribution, and reproduction in any medium, provided the original work is properly cited.


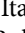

Chief Editor

Stefano Bellucci , Italy

















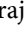
















Associate Editors

Ilaria Armentano, Italy
Stefano Bellucci , Italy
Paulo Cesar Morais , Brazil
William Yu , USA

Academic Editors

Buzuayehu Abebe, Ethiopia
Domenico Acierno , Italy
Sergio-Miguel Acuña-Nelson , Chile
Katerina Aifantis, USA
Omer Alawi , Malaysia
Nageh K. Allam , USA
Muhammad Wahab Amjad , USA
Martin Andersson, Sweden
Hassan Azzazy , Egypt
Ümit Ağbulut , Turkey
Vincenzo Baglio , Italy
Lavinia Balan , France
Nasser Barakat , Egypt
Thierry Baron , France
Carlos Gregorio Barreras-Urbina, Mexico
Andrew R. Barron , USA
Enrico Bergamaschi , Italy
Sergio Bietti , Italy
Raghvendra A. Bohara, India
Mohamed Bououdina , Saudi Arabia
Victor M. Castaño , Mexico
Albano Cavaleiro , Portugal
Kondareddy Cherukula , USA
Shafiul Chowdhury, USA
Yu-Lun Chueh , Taiwan
Elisabetta Comini , Italy
David Cornu, France
Miguel A. Correa-Duarte , Spain
P. Davide Cozzoli , Italy
Anuja Datta , India
Loretta L. Del Mercato, Italy
Yong Ding , USA
Kaliannan Durairaj , Republic of Korea
Ana Espinosa , France
Claude Estournès , France
Giuliana Faggio , Italy
Andrea Falqui , Saudi Arabia

Matteo Ferroni , Italy
Chong Leong Gan , Taiwan
Siddhartha Ghosh, Singapore
Filippo Giubileo , Italy
Iaroslav Gnilitzkiy, Ukraine
Hassanien Gomaa , Egypt
Fabien Grasset , Japan
Jean M. Greneche, France
Kimberly Hamad-Schifferli, USA
Simo-Pekka Hannula, Finland
Michael Harris , USA
Hadi Hashemi Gahruei , Iran
Yasuhiko Hayashi , Japan
Michael Z. Hu , USA
Zhengwei Huang , China
Zafar Iqbal, USA
Balachandran Jeyadevan , Japan
Xin Ju , China
Antonios Kellarakis , United Kingdom
Mohan Kumar Kesarla Kesarla , Mexico
Ali Khorsand Zak , Iran
Avvaru Praveen Kumar , Ethiopia
Prashant Kumar , United Kingdom
Jui-Yang Lai , Taiwan
Saravanan Lakshmanan, India
Meiyong Liao , Japan
Shijun Liao , China
Silvia Licoccia , Italy
Zainovia Lockman, Malaysia
Jim Low , Australia
Rajesh Kumar Manavalan , Russia
Yingji Mao , China
Ivan Marri , Italy
Laura Martinez Maestro , United Kingdom
Sanjay R. Mathur, Germany
Tony McNally, United Kingdom
Pier Gianni Medaglia , Italy
Paul Munroe, Australia
Jae-Min Myoung, Republic of Korea
Rajesh R. Naik, USA
Albert Nasibulin , Russia
Ngoc Thinh Nguyen , Vietnam
Hai Nguyen Tran , Vietnam
Hiromasa Nishikiori , Japan

Sherine Obare , USA
Abdelwahab Omri , Canada
Dillip K. Panda, USA
Sakthivel Pandurengan , India
Dr. Asisa Kumar Panigrahy, India
Mazeyar Parvinzadeh Gashti , Canada
Edward A. Payzant , USA
Alessandro Pegoretti , Italy
Oscar Perales-Pérez, Puerto Rico
Anand Babu Perumal , China
Suresh Perumal , India
Thathan Premkumar , Republic of Korea
Helena Prima-García, Spain
Alexander Pyatenko, Japan
Xiaoliang Qi , China
Haisheng Qian , China
Baskaran Rangasamy , Zambia
Soumyendu Roy , India
Fedlu Kedir Sabir , Ethiopia
Lucien Saviot , France
Shu Seki , Japan
Senthil Kumaran Selvaraj , India
Donglu Shi , USA
Muhammad Hussnain Siddique , Pakistan
Bhanu P. Singh , India
Jagpreet Singh , India
Jagpreet Singh, India
Surinder Singh, USA
Thangjam Ibomcha Singh , Republic of Korea
Korea
Vidya Nand Singh, India
Vladimir Sivakov, Germany
Tushar Sonar, Russia
Pingan Song , Australia
Adolfo Speghini , Italy
Kishore Sridharan , India
Marinella Striccoli , Italy
Andreas Stylianou , Cyprus
Fengqiang Sun , China
Ashok K. Sundramoorthy , India
Bo Tan, Canada
Leander Tapfer , Italy
Dr. T. Sathish Thanikodi , India
Arun Thirumurugan , Chile
Roshan Thotagamuge , Sri Lanka

Valeri P. Tolstoy , Russia
Muhammet S. Toprak , Sweden
Achim Trampert, Germany
Tamer Uyar , USA
Cristian Vacacela Gomez , Ecuador
Luca Valentini, Italy
Viet Van Pham , Vietnam
Antonio Vassallo , Italy
Ester Vazquez , Spain
Ajayan Vinu, Australia
Ruibing Wang , Macau
Magnus Willander , Sweden
Guosong Wu, China
Ping Xiao, United Kingdom
Zhi Li Xiao , USA
Yingchao Yang , USA
Hui Yao , China
Dong Kee Yi , Republic of Korea
Jianbo Yin , China
Hesham MH Zakaly , Russia
Michele Zappalorto , Italy
Mauro Zarrelli , Italy
Osman Ahmed Zeleke, Ethiopia
Wenhui Zeng , USA
Renyun Zhang , Sweden





Contents

Optimization of Synthesis Conditions of β -FeOOH Nanorods towards Antimicrobial Benefits

Fatemeh Mohammadi , Salme Amiri , Esmail Mirzaei , and Ahmad Gholami 





Research Article (13 pages), Article ID 7012012, Volume 2022 (2022)

Optimized Synthesis of Xanthan gum/ZnO/TiO₂ Nanocomposite with High Antifungal Activity against Pathogenic *Candida albicans*

Fatemeh Ghorbani , Pourya Gorji , Mohammad Salmani Mobarakeh , Hamid Reza Mozaffari , Reza Masaeli , and Mohsen Safaei 

Research Article (10 pages), Article ID 7255181, Volume 2022 (2022)





Antibacterial, Cytotoxic, and Cellular Mechanisms of Green Synthesized Silver Nanoparticles against Some Cariogenic Bacteria (*Streptococcus mutans* and *Actinomyces viscosus*)

Hanaa Ghabban , Sultan F. Alnomasy , Hamdan Almohammed , Ohoud M. Al Idriss , Sameh Rabea , and Yasir Eltahir 

Research Article (8 pages), Article ID 9721736, Volume 2022 (2022)

Research Article

Optimization of Synthesis Conditions of β -FeOOH Nanorods towards Antimicrobial Benefits

Fatemeh Mohammadi ¹, Salme Amiri ², Esmail Mirzaei ² and Ahmad Gholami ³

¹Biotechnology Research Center, Shiraz University of Medical Sciences, Shiraz, Iran P.O. Box 71348-14336

²Department of Medical Nanotechnology, School of Advanced Medical Sciences and Technologies, Shiraz University of Medical Sciences, Shiraz, Iran P.O. Box 71348-14336

³Pharmaceutical Sciences Research Center, Shiraz University of Medical Sciences, Shiraz, Iran P.O. Box 71348-14336

Correspondence should be addressed to Ahmad Gholami; gholami@sums.ac.ir

Received 13 September 2021; Revised 14 August 2022; Accepted 24 August 2022; Published 24 September 2022

Academic Editor: P. Davide Cozzoli

Copyright © 2022 Fatemeh Mohammadi et al. This is an open access article distributed under the Creative Commons Attribution License, which permits unrestricted use, distribution, and reproduction in any medium, provided the original work is properly cited.

FeOOH nanoparticles have recently appealed to wide-ranging applications due to their physicochemical properties and size-tunable synthesis; however, a few studies were performed on the antimicrobial potentials of iron oxyhydroxide nanoparticles. In this regard, we aimed to design various synthesis experiments to optimize the fabrication of β -FeOOH nanorods (NRs) with a desirable size of NRs and high antimicrobial potential. For this purpose, ten experiments were designed by manipulating reaction conditions of the standard hydrolysis method, including the initial concentration of ferric ions, reaction time, reaction temperature, and different concentrations of surfactants of PEI and PEG as process control agents. The structural characteristics of prepared NRs were analyzed using FE-SEM, FTIR, and XRD. The ImageJ software was also used to measure the length, width, and aspect ratio of NRs. Five microbial species, including the Gram-positive and Gram-negative bacteria and fungi species, were applied to investigate the antimicrobial potentials of NRs. The initial concentration of ferric ions revealed a dominant effect in NRs' morphology, though other reaction conditions also played essential roles. The crystal structure of NRs was preserved in all synthesis experiments (β -phase) due to using the same iron salt precursors. The synthesized NRs exhibited dose-dependent antimicrobial activities against all tested microbial species. Additionally, the presence of surfactants exhibited an excellent capability of controlling effects on the size and growth pattern of NR crystals and improving their antimicrobial potentials; PEI could also be more effective on the antimicrobial efficacy of final NRs. Besides, our findings exhibited an inverse correlation between aspect ratio and antimicrobial potentials of β -FeOOH NRs. To sum up, it seems that optimization of synthesis conditions could provide tunable size and structure patterns of β -FeOOH NRs to achieve a promising tool for biomedical applications, particularly in combat with resistant microbial species, though further studies are needed in this regard.

1. Introduction

Antimicrobial resistance, described as a defense mechanism of bacteria or fungi to protect against antimicrobial agents, is one of the ten leading global health issues recommended to track in 2021, based on recent reports by the World Health Organization [1]. It can be associated with over and misuse of conventional antibiotics, the inefficiency of current antimicrobial agents due to low stability and solubility, and possible side effects. Accordingly, new innovative strategies are in high demand to overcome these ever-increasing concerns

[2]. For this purpose, novel nanoscale systems for targeted antibiotic drug delivery and some potent antimicrobial nanoparticles (NPs) emerged with great antimicrobial efficacies against various resistant microorganisms [3]. Various nanomaterials have been studied in this regard, like metal NPs, transition metal dichalcogenide nanostructures, and carbon-based nanomaterials, in diverse forms, from single-phase particles to hybrid structures and nanosheets [4–7].

Iron nanoparticles (INPs) are one important and widely used metal NPs due to their unique physicochemical properties, high biocompatibility, low toxicity, and simple synthesis

pathways [8–10]. INPs have received much attention in the last two decades for wide biomedical applications as imaging and therapeutic agents such as magnetic resonance imaging (MRI) and magnetic hyperthermia, gene and drug delivery, biosensor and immunoassay, antimicrobial functions, tissue engineering, cancer therapy, and theranostic approaches [11–14]. Iron oxyhydroxide (FeOOH), as one type of INP, recently appealed to different applications, including water treatment and degradation of organic pollutants due to their potential to generate reactive oxygen species, photocatalyst, solar cell, and ion batteries [15, 16]. According to crystalline structures, it can be found in various nanoscale polymorphs containing goethite (α -FeOOH), akaganeite (β -FeOOH), lepidocrocite (γ -FeOOH), and ferroxhyte (δ -FeOOH) [17]. In recent years, there has been growing interest in optimizing the synthesis of FeOOH NPs, especially in β -phase, to apply in wide applications. The standard synthetic nanostructure of β -FeOOH is nanorods (NRs) which can be achieved by hydrolysis of ferric ions in an aquatic environment and chloride ions [17].

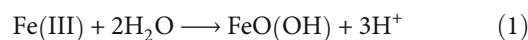
One of the promising applications of β -FeOOH NRs is the capability of converting to magnetic iron oxide NRs. The fabrication of elongated iron oxide NPs directly from iron salts takes complicated procedures due to their preferential cubic orientation in the crystal growth process [18]. This conversion can be implemented by using a reducing agent or calcinating FeOOH NRs in high temperatures above 400°C [19]. Besides, the composites of FeOOH NRs revealed high efficiency in potassium and lithium-ion batteries due to their excellent electrochemical performances, high capacity, and decent cycling stability [20]. Nanoellipsoids of FeOOH were also suggested as food-grade NPs with a good source of ferrous ions in food fortification and supplements [21]. In addition, there is a vast amount of literature on the antimicrobial benefits of FeOOH NPs individually or in a composite of nanostructures incorporated with other elements. Nanocomposites of FeOOH/AlOOH containing iron oxyhydroxide and aluminum oxyhydroxide NPs presented synergistic antimicrobial effects against Gram-positive and Gram-negative bacterial strains without any significant cytotoxicity [22]. Moreover, iron-based nanopillar arrays consisting of Fe₂O₃ and FeOOH NPs exhibited good antimicrobial effects against tested bacteria and fungi strains, which suggested ideal surface disinfection and their ability to grow in various substrates [23]. β -FeOOH NRs have also exhibited high inhibitory effects on biofilm formation, the leading cause of bacterial antibiotic resistance [24].

Despite this interest, no one, as far as we know, has optimized the synthesis of β -FeOOH NRs for antimicrobial applications by considering the influential roles of particle size and concentration of NPs along with preserved morphology. Previous evidence indicated that the initial concentration of iron ions and reaction conditions such as reaction times could significantly effect on characteristics of NRs, particularly the length of rods which, unlike NRs' width, is much tuneable as a result of these changes [25]. Accordingly, we aimed to design different experiments to synthesize β -FeOOH NRs by manipulating reaction conditions of com-

mon hydrolysis approaches with different concentrations of iron salt precursors to obtain a potent antimicrobial agent. The antimicrobial evaluation of synthesized NPs was assessed against five microbial species, including the Gram-positive and Gram-negative bacteria and fungi species. In addition, earlier studies highlighted that the presence of additional compounds as surfactants, including polymers such as polyethyleneimine, carbohydrates, salts, acids, and also algal culture supernatant, could improve the fabrication of FeOOH NRs by controlling size, the growth pattern of crystals, and stability [18]. Therefore, we also carried out the synthesis of FeOOH NRs in the presence of two widely used chemical polymers, polyethyleneimine (PEI) and polyethylene glycol (PEG), in different concentrations to evaluate their effects on synthesis process and antimicrobial activities of final NRs.

2. Materials and Methods

2.1. Synthesis. FeOOH NRs were generally synthesized by the hydrolysis of ferric ions in aqueous environments, as shown in



A total of ten experiments were designed based on previous studies to optimize the synthesis of β -FeOOH NRs with the highest antimicrobial properties. Parameters considered in designed experiments are as follows, which exhibited significant roles in morphology and size of final NRs: initial concentration of ferric ions; different concentrations of surfactant, PEI, and PEG; and reactions time and temperature. The second compounds containing PEI and PEG were employed in the one-pot method to control the variables of the synthesis process. Firstly, a 40 mL homogeneous ferric chloride solution was prepared with certain concentrations of ferric chloride hexahydrate (FeCl₃·6H₂O) and deionized water. The surfactant compounds were employed to control the size of final NPs. So, PEG with final concentrations of 1, 3, and 6% *w/v* and PEI with concentrations of 0.25, 0.5, and 1.25% *w/v* were added. Then, the mixture was heated to 80–120°C for 2–12 h under sealed conditions (Table 1). Brownish suspension of synthesized NPs was centrifuged (10000 rpm, 30 min) and rinsed three times with deionized water, and finally, obtained precipitates were dried at 60°C for 24 h and stored at 4°C. During the synthesis process, the color change was observed from light orange to deep brown, confirming the fabrication of β -FeOOH NRs [26].

2.2. Characterizations. FeOOH NRs synthesized with and without surfactants were characterized by field emission scanning electron microscopy (FE-SEM, Mira3, XMU, Germany) and energy-dispersive X-ray spectroscopy detector and mapping (EDX, Mira III, TESCAN) to determine morphology, size distribution, and qualitative analysis; X-ray diffraction (XRD, Siemens D5000, Karlsruhe, Germany) to analyze crystal structures and crystallite size; zeta potential analysis using Zetasizer (Nano ZS-90, Malvern Instruments, UK) to assay surface charge of final NRs; and Fourier

TABLE 1: Mean size of FeOOH nanorods, length, width, and aspect ratio based from FE-SEM results along with crystallite size of nanorods measured by using XRD data.

Experiment	FeCl ₃ ·6H ₂ O (gr/mL)	Temperature (°C)	Time (hours)	Surfactant concentration (%w/v)	Length (nm)	Width (nm)	Aspect ratio: length/width	Crystallite size (nm)
1	0.0027	80	10	—	125	34	3.676	23
2	0.0324	80	2	—	120	30	4	18
3	0.05	120	4	—	425	85	5	26
4	0.008	80	12	PEG-1%	216	74	2.919	24
5	0.008	80	10	PEG-3%	165	49	3.367	34
6	0.008	80	2	PEG-3%	129	36	3.58	23
7	0.008	80	10	PEG-6%	154	44	3.5	20
8	0.008	120	4	PEI-0.25%	124	88	1.409	28
9	0.15	120	4	PEI-0.5%	772	103	7.495	21
10	0.15	120	4	PEI-1.25%	661	90	7.34	26

transform infrared spectroscopy (FTIR Spectroscope, Vertex 70, Bruker, Germany) to identify chemical bonds in molecules and assess their chemical properties. The FTIR spectrum of NPs was recorded in the range of 400–4000 cm⁻¹ at room temperature using the standard KBr pellet method. The Fe content of each sample was measured by Inductively Coupled Plasma Optical Emission (ICP-OES) spectroscopy (ICP-OES Spectrometer, Perkin Elmer Optima 7300 DV, USA) before treating microorganisms. The ImageJ software, open-source image analysis software, was also used for the measurement of length, width, and aspect ratio of NRs.

2.3. Antimicrobial Assay. The antimicrobial potential of as-prepared β -FeOOH NRs was assessed by microdilution methods, based on the clinical and laboratory standard institute (CLSI, 2019), against Gram-positive and Gram-negative bacterial species and a common fungal pathogen of humans. For this purpose, *Staphylococcus aureus* (*S. aureus*) PTCC 1112, *Enterococcus faecalis* (*E. faecalis*) PTCC 1778, *Escherichia coli* (*E. coli*) PTCC 1399, *Salmonella typhi* (*S. typhi*) PTCC 1609, and fungal species of *Candida albicans* (*C. albicans*) PTCC 5027 were purchased from Persian type culture collection center. Bacterial species were cultured in BHI media at 37°C with 200 rpm agitation, and *C. albicans* was cultured in an RPMI culture medium. The microdilution method was applied to achieve the minimum inhibitory concentration MIC of NRs and quantitatively report their antimicrobial potentials against microbial strains. The MIC value was considered the lowest concentration of NRs able to inhibit 90% of microbial growth after overnight incubation.

10 μ L of prepared bacterial suspension containing about 5×10^6 CFU/mL inoculated to the wells of a 96-well microplate containing 90 μ L medium with the concentration of 500, 250, 125, 62.5, 31.25, 16.12, 8, and 4 μ g/mL of each synthesized NRs. After 24 hours of incubation of microplates at 37°C, the optical density of all wells was measured by a microplate reader (PowerWave XS2, BioTek Instruments Inc., US) at 600 nm. Control groups were defined as wells containing medium with the same microbial inoculation without any NRs and blank groups containing medium without microbial inoculation or NRs.

3. Results and Discussion

Nanostructures of akaganeite are generally found in elongated orientations such as rods or ellipsoids, which can be formed in iron- and chloride-rich environments and heating to at least 80°C. In contrast, this hydrothermal reaction prolongs at least six months at room temperature [27]. Through the akaganeite synthesis process, as Fe salts dissolve in water, Fe³⁺ ions will make a complex with water molecules and from [Fe(H₂O)₆]³⁺. Then, the synthesis process is continued by hydrolysis reaction in two steps, release of protons from water molecules and formed double octahedral units via Fe–OH–Fe bonds, which can interact strongly or weakly with various anions, and form various morphology and size of FeOOH nanorods in the polymerization step [28]. Thus, the type of anions of ferric salt plays a determinative role in the final size and crystallization of the products. Yue et al. described the synthesis of β -FeOOH NPs from different iron salts in an experimental and theoretical study and suggested FeCl₃ for achieving β -FeOOH NRs [29]. According to their evidence, firstly, hydrothermal reaction arranges FeO₆ octahedral units to form FeOOH seeds, double octahedral units, and finally lattices.

During the growth process, chloride ions are adsorbed on the surface of FeOOH lattices due to high electronegativity and direct the growth of NPs through elongated structures by strong interactions (Figure 1). This study highlighted the significant effects of various anions of ferric salts on the morphology and size of obtained FeOOH NPs. FeCl₃ salt leads to the formation of FeOOH NRs in the β phase. However, other salts of iron provide different morphology of FeOOH NPs. Fe(NO₃)₃ helps the synthesis of spherical goethite NPs (α -FeOOH), and the Fe₂(SO₄)₃ salt leads to produce amorphous FeOOH NPs with irregular morphology [29].

There is a considerable amount of optimization studies on NP synthesis using almost the same synthesis protocols, obtaining distinct characteristics and properties, including size, morphology, crystallinity, and biological activities. It has been performed just with some simple and facile changes in reaction conditions or precursors without any remarkable

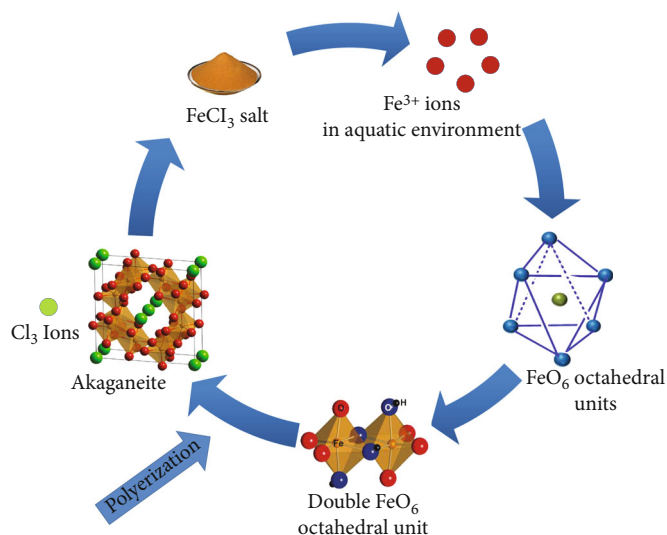


FIGURE 1: Schematic diagram illustrating the synthesis mechanism of β -FeOOH nanorod structures from ferric ions in the aquatic environment.

modifications in the protocol of synthesis. Sayed and Polshettiwar reported the synthesis of iron oxide nanoparticles in six different morphologies denoted as follows, based on the same protocols with simply changing precursor iron salts: distorted, nanocubes, porous spheres, and self-oriented flower shapes [30]. Moreover, Moradpoor et al. described nine different synthesis experiments of cobalt oxide NPs to obtain an optimal antibacterial agent. In this case, the same protocol was applied in experiments with changes in the reaction conditions, such as stirring time and concentrations of precursors containing cobalt salts and reducing agents [31].

In this work, we aimed to optimize the fabrication of β -FeOOH NRs to achieve the desired size along with the high potent antimicrobial activity. Although FeOOH NPs can be formed in rod-like morphologies without using additive compounds, however, appropriate surfactants can facilitate the synthetic process and control the growth pattern of crystals in uniform size and shape [32]. Accordingly, we applied PEG and PEI polymers as process control agents to the one-pot synthesis of β -FeOOH NRs and four Gram-positive and Gram-negative bacterial strains, including *S. aureus*, *E. faecalis*, *E. coli*, and *S. typhi*, and one of the pathogenic fungal species, *C. albicans*, to find the best antimicrobial potent NR of as-prepared NPs.

3.1. Characterizations. Figure 2 displays the FE-SEM micrograph of synthesized NPs achieved from designed experiments. All NPs exhibited elongated and rod-like morphology with almost good monodispersity. The mean size and aspect ratio of NRs were evaluated by size measurement of at least 100 NPs selected at random per condition by the ImageJ software. Table 1 illustrates the measured length and width mean sizes and aspect ratio per experiment individually.

As indicated in previous literature, the concentration of ferric salts plays a defining role in the synthesis of β -FeOOH NPs by controlling the growth of nanocrystals. Increasing

the concentration of ferric ions leads to an increase in the length of NRs without significant width change and subsequently elevated aspect ratio since a higher concentration of ferric salts provides more ferric precursor along with more acidic pH, facilitating parameters in the hydrolysis process and further growth of NRs [28, 33]. In this regard, we also found that increasing the concentration of ferric ions raises the length of NRs without a significant change in aspect ratio (Table 1). Moreover, surfactants are considered a decisive factor in NR synthesis by tuning the morphology [34, 35]. As shown in the results, more concentration of PEG leads to a decreased size of final NRs without significant change in aspect ratio, 3.5 compared to 2.9 (Exp. 7 to Exp. 4). Kasparis et al. also confirmed the significant role of surfactants on the morphology of FeOOH nanorods. A high concentration of PEI revealed significant decreases in NPs with well-preserved crystal structure and aspect ratio [18]. However, unlike the expected effects of surfactants, the increase of PEI concentrations in Exp. 9 and 10 made their particle size larger than Exp. 8 and remarkably changed in aspect ratio (7.34 compared to 1.41). This reveals the dominant role of higher ferric ions concentration in synthesis reaction that minimizes the surfactant effects, increasing the length of NRs and, after that, increasing the aspect ratio.

Nevertheless, reductive effects of PEI on the mean size of NPs can be observed in NPs obtained from Exp. 10 compared to Exp. 9. All of the synthesis conditions were similar in the two experiments except for the increased concentration of PEI surfactant in Exp. 10, providing a smaller size of NPs with a similar aspect ratio. Additionally, we found that although Exp. 7 was carried out in the presence of a higher concentration of PEG compared to Exp. 6, however, size of NPs increased without a change in aspect ratio. It can result from an increased time reaction of up to 10 hours that could improve the growth of crystals and provide a larger size of NRs. Notably, the aspect ratio did not change significantly in this experiment, and the size change was limited due to the tuning effects of surfactants.

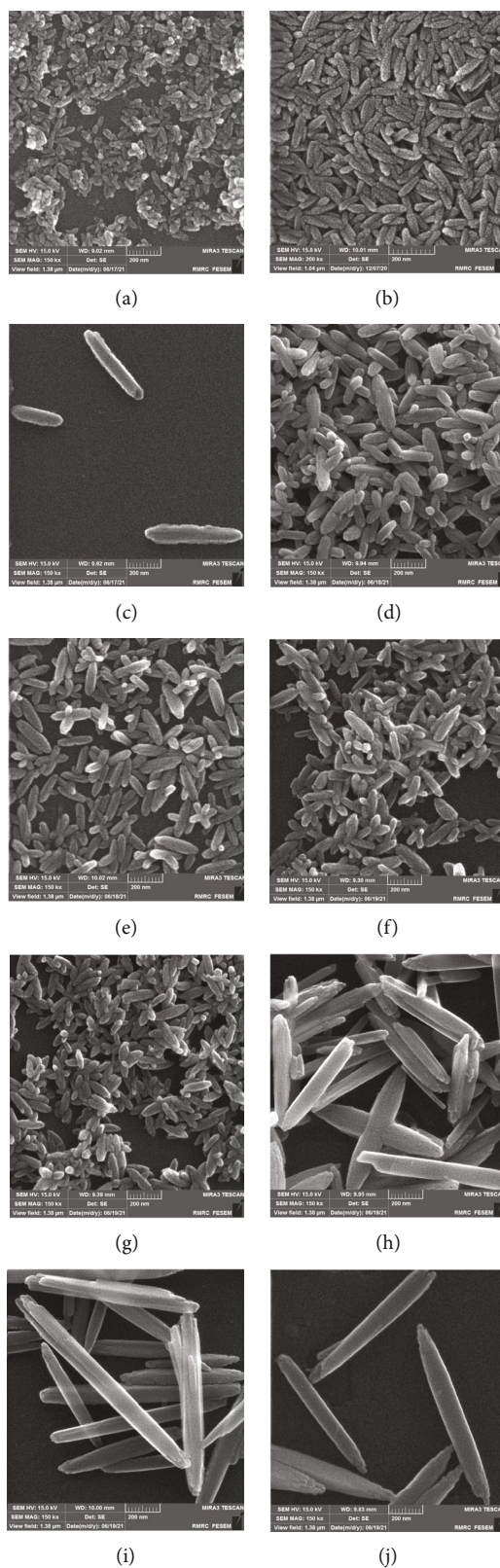


FIGURE 2: FE-SEM micrographs of the β -FeOOH nanorods synthesized by various synthesis experiments: (a–j) Exp. 1–10, respectively.

As proposed in previous studies, the evidence we found highlights the influential role of surfactants like PEG and PEI in controlling the particle size and improving the size

distribution of final β -FeOOH NRs during fabrication. PEG molecules favor the fabrication of smaller sizes of β -FeOOH NRs, as suggested by Wei et al. The possible

TABLE 2: Effects of various synthesis parameters on the structural properties of prepared β -FeOOH nanorods.

Structural properties of final NPs	Kind of Fe salts (anions)	Fe salt concentration	Reaction time	Surfactant concentration
Morphology (size)	*	*	*	*
Aspect ratio	*	*	—	—
Crystal structure	*	—	—	—

*Dependent-Independent.

mechanisms that PEG surfactant firmly coordinated with ferric ions (Fe^{3+}) through OH functional groups were proposed to explain this effect, which prevents nuclei aggregation and subsequently achieves the smaller size of β -FeOOH NRs. Furthermore, PEG surfactant avoids the aggregation of final synthesized NRs and maintains the size and morphology [34].

In addition, in earlier investigations, the role of PEI polymer in improving the morphology of metal oxide NRs and reducing their diameters and length has been argued in detail. For this purpose, PEI as a cation surfactant was suggested to limit the lateral growth of NRs remarkably by adsorbing on the negatively charged lateral facets of NRs during the synthesis process owing to electrostatic interaction. Moreover, amino groups of this surfactant coordinated with NRs, which led to obtaining NRs with smaller diameters than synthesized NPs without surfactants [36]. Besides, PEI was argued to be the controlling agent of length and width of β -FeOOH NRs by Mohapatra et al. The adsorption of PEI molecules on the lateral plan of NRs was suggested for the mechanism of this action [37].

Reaction time is one of the other factors that can affect the morphology of FeOOH NRs. Kasparis et al. reported that the increasing reaction time from 30 min to 4 hours made larger NRs without effects on the aspect ratio [18]. In this study, we also found that NRs achieved larger size with preserved aspect ratio by extending reaction times from 2 to 10h in the presence of a consistent concentration of PEG and ferric ions (Exp. 5 compared to Exp. 6), even though this size change was limited due to presence of surfactant. In addition, while the reaction time of Exp. 1 was more than Exp. 3, obtained NPs did not show a larger size and even revealed a smaller size and aspect ratio. These findings confirm the dominant effect of ferric ions concentration, as the concentration of iron salts applied more in Exp. 3.

Our findings appeared well substantiated by previous studies on effective parameters for synthesis reactions containing ferric ion concentration, presence of surfactant, and reaction time (Table 2). Findings suggest that ferric ion concentration is the dominant factor in the morphology of NRs. Also, surfactants such as PEI and PEG can be good candidates to tune the size and aspect ratio of β -FeOOH NRs efficiently. The aspect ratio is independent of all factors except ferric ion concentrations. Moreover, in the consistence of other synthesis parameters, time reactions can cause the overgrowth of NRs; therefore, it should also be considered to tune NR morphology. Furthermore, EDX spectroscopy was performed for qualitative analysis and chemical characterization of β -FeOOH NRs prepared with and without the presence of surfactants, as revealed in Figure 3. As shown

in the results, a desirable percentage of Fe and O was obtained in all NRs, which confirms the successful formation of β -FeOOH NRs. Moreover, the contents of C, N, and O in the results related to NRs obtained from synthetic EXP 4-10 indicated the surface functionalization of NRs by PEG and PEI.

The FTIR spectrum of prepared NRs is exhibited in Figure 4. According to previous studies, specific characteristic peaks should be assessed to analyze and confirm the appropriate synthesis of FeOOH NPs chemically. The absorption peaks in the 300 to 700 cm^{-1} have frequently been assigned to fundamental vibrational bands of inorganic ions [3]. FeO_6 octahedral units of β -FeOOH NRs are identified by characteristic peaks of two prominent vibration bands, FeO and OH groups. The vibration of FeO groups of octahedral units was observed as Fe–O bending vibrations at about 400 cm^{-1} and Fe–O stretching vibrations containing symmetrical stretching bands from 435 to 495 cm^{-1} and asymmetrical stretching bands at 647 to 700 cm^{-1} [28, 38, 39]. As shown in Figure 4, the characteristic absorption peaks related to Fe–O bands of octahedral sites are perceptible between 400 and 700 cm^{-1} in all sample graphs. In addition, structural OH bands as Fe–OH in the octahedral site are recognized by bending vibration at $\sim 818 \text{ cm}^{-1}$. Also, O–H...O bending vibration in Fe–O–OH bands is reported between 840 and 850 cm^{-1} [28, 39]. The FTIR spectrum of all samples represents the prominent absorption peaks in the range of 820–850 cm^{-1} , confirming the existence of structural OH groups in octahedral units of FeOOH NRs. In line with former findings, the stretching and bending vibrational bands of surface hydroxyl groups were found at a range of about 3390–3490 and 1620–1650 cm^{-1} , respectively, corresponding to possible adsorbed water molecules in FeOOH NPs [14, 38]. The additional bands detected in the region of 1550–1350 cm^{-1} and 2850–3000 cm^{-1} are assigned to artefacts of the preparation or organic contaminants. However, some evidence considered the absorption bands located in 1350 to 1490 cm^{-1} peculiar to β -FeOOH NPs and convenient to differentiate it from other phases [39]. Additionally, surface functionalization of NRs with PEG and PEI surfactants could be confirmed by the characteristic peaks related to C–H and N–H vibration of hydrocarbon chains and the amine groups of the polymer structures in the FTIR spectrum of NRs (Figure 4). The corresponding peaks of the stretching and bending vibration of C–H bond appeared at 2800–3000 cm^{-1} and 1300–1500 cm^{-1} , respectively [40–43], as our findings also illustrated these absorption ranges as small peaks (Figures 4(b) and 4(c)). Moreover, previous findings reported that the absorption peak range of 1500–1650 cm^{-1} and 3000–3400 cm^{-1} were ascribed to N–H

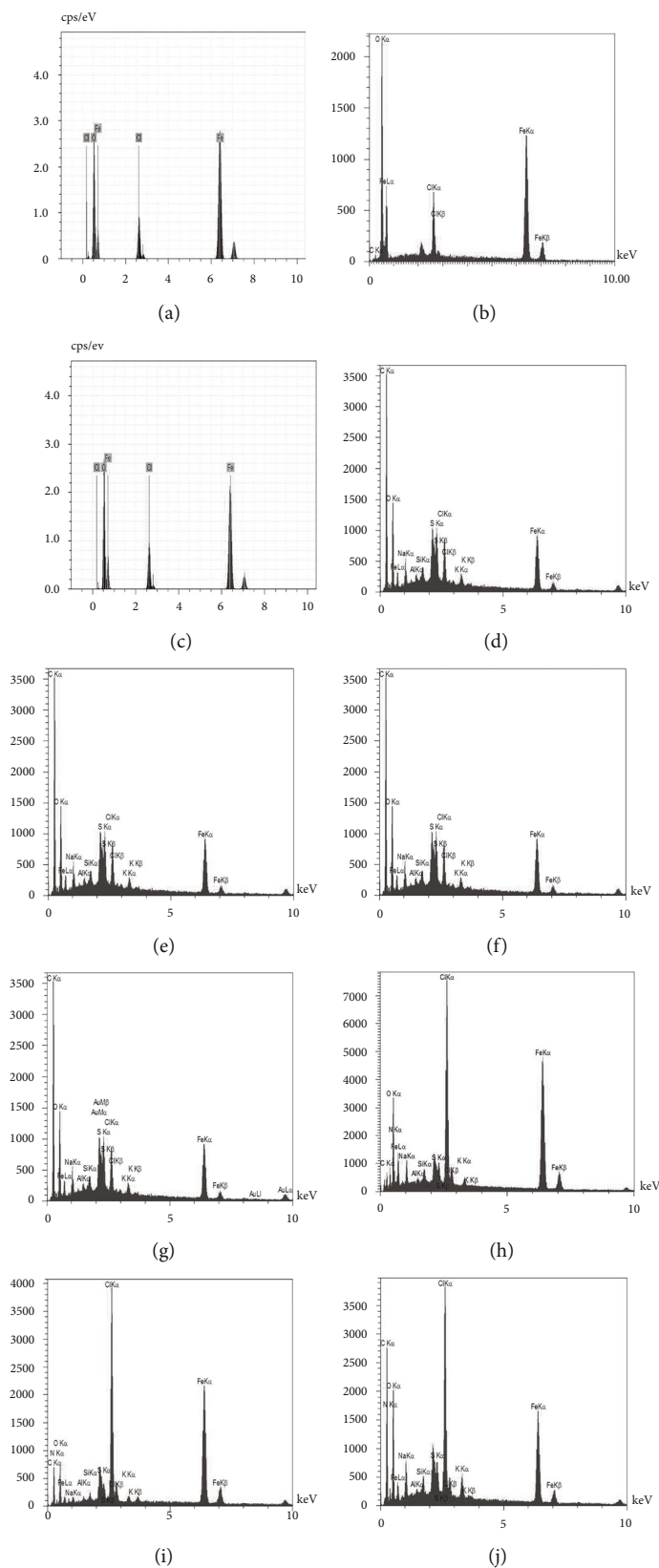


FIGURE 3: EDX pattern of β -FeOOH nanorods synthesized by various synthesis experiments. (a–c) Exp. 1–3, NRs without surface functionalization. (d–g) Exp. 4–7, NRs with PEG surface functionalization. (h–j) Exp. 8–10, NRs with PEI surface functionalization.

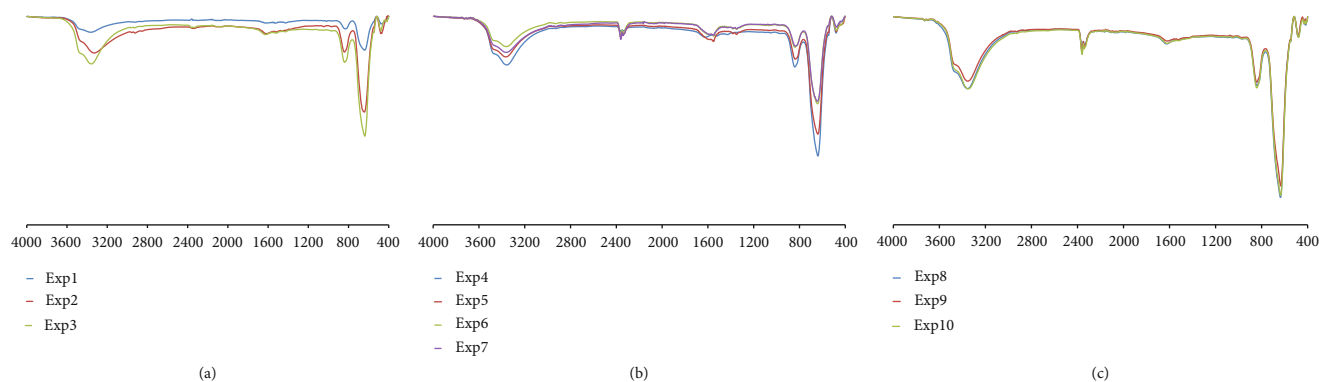


FIGURE 4: FTIR spectra of the β -FeOOH nanorods prepared by various synthesis experiments. (a) Exp. 1-3, NRs without surface functionalization. (b) Exp. 4-7, NRs with PEG surface functionalization. (c) Exp. 8-10, NRs with PEI surface functionalization.

bending and stretching vibration region related to the amine groups of PEI molecules [44–46], which are illustrated in Figure 4(c) as a broad peak in the region of 3000 to 3500 cm^{-1} that seems to be overlapped with the peaks of O–H stretching vibrations.

The XRD patterns FeOOH NRs as prepared through different designed experiments of the one-pot hydrothermal method are provided in Figure 5. All of the diffraction peaks were consistent well with the typical values of β -FeOOH NR pattern based on the Joint Committee of Powder Diffraction Standards (JCPDS) database (reference code: 00-034-1266), related to the tetragonal body-centered crystal structure of β -FeOOH with lattice parameters: $a = b = 10.535 \text{ \AA}$, $c = 3.03 \text{ \AA}$, and $V = 336.29 \text{ \AA}^3$. As shown in Figure 5, all of the reflection peaks were well indexed to a similar tetragonal phase of β -FeOOH and in line with previous reports [47]; the crystal structure of β -FeOOH NRs is independent of synthesis parameters manipulated in this work, including ferric ion concentration, surfactant concentration (PEG and PEI), temperature, and time reaction.

In this regard, a similar experiment reported that the presence and concentration of size-controlling agents such as PEI and different HCl molarities have no significant impacts on the crystal structure of prepared β -FeOOH NRs [18, 48]. Similar results were also confirmed that the β -FeOOH crystals are independent of the concentration of ferric ions in hydrolysis synthesis [28, 33]. Moreover, Parameshwari et al. reported that a sufficient amount of dextrose as a chelating agent is required to acquire a stable and single phase of β -FeOOH in the coprecipitation method. The coexistence of the secondary phase of FeOOH occurred in low concentrations of dextrose [38].

In addition, in this study, the crystallite size of NRs was measured using XRD data, which revealed a narrow-range difference between all samples, 18–34 nm. It implies that various synthesis conditions could not significantly impact the crystallite size of NRs, despite their remarkable impacts on the length and width of final NRs (Table 1). Before assessing the antimicrobial effects of synthesized NRs, each sample's surface charge and iron concentration were determined by zeta potential analysis and ICP-OES spectroscopy, as shown in Table 3. The results noticeably indicated the positive surface charge of β -FeOOH NRs prepared in the presence of

PEI surfactant (Exp. 8–10), which increased 15.5 ± 5.8 to 62.9 ± 0.6 due to the rise of PEI concentration from 0.25–1.25% w/v , while zeta potential measurement showed the negative surface charge of β -FeOOH NRs synthesized in the presence of PEG or without surfactant agents (Exp. 1–7). Consistent with previous evidence, this positive surface charge owing to surface modification of NPs could play a significant role in their biological behaviors, particularly antimicrobial activities [49, 50]. Moreover, according to ICP data, the concentration of Fe was found within a narrow range of concentration in all samples, between 212.68 and 307.38 $\mu\text{g/mL}$ (Table 3). The impact of this difference between the iron content of samples seems negligible in evaluating NRs' antimicrobial properties.

3.2. Antimicrobial Assay. Antibacterial and antifungal activities of prepared β -FeOOH NRs synthesized with and without surfactants were evaluated by microdilution against five pathogenic microorganism species, including *S. aureus*, *E. faecalis*, *E. coli*, *S. typhi*, and *C. albicans*. Figure 6 represents the viability percentage of microorganisms treated by 500, 250, 125, 62.5, 31.25, 16.12, 8, and 4 $\mu\text{g/mL}$ of each synthesized NRs. All NRs exhibited dose-dependently inhibitory effects on microbial growth; higher concentrations led to more growth inhibition, as shown in the results. According to MIC value (Table 4), Gram-negative species demonstrated more susceptibility than Gram-positive bacterial species; *S. typhi* showed the most and *S. aureus* and *E. faecalis* the least susceptibility to NRs. Gram-positive bacteria such as staphylococci, enterococci, and pneumococci are currently known as pathogens of great concern due to their intrinsic virulence inducing various infections and exceptionally high multidrug resistance, which should be addressed before long [51]. Based on the results, Synthesized NRs could inhibit the growth of *S. aureus* and *E. faecalis*, mostly just in high concentrations.

The impacts of surfactant presence on the antimicrobial properties of final NRs were evaluated by comparing the results of Exp. 1, 6, and 8, NRs with fairly similar length sizes that were obtained, respectively, in the absence of any surfactants and in the presence of PEG and PEI. NRs synthesized in the absence of surfactants exhibited the least antimicrobial effects on all tested microbial species; however, surfactant

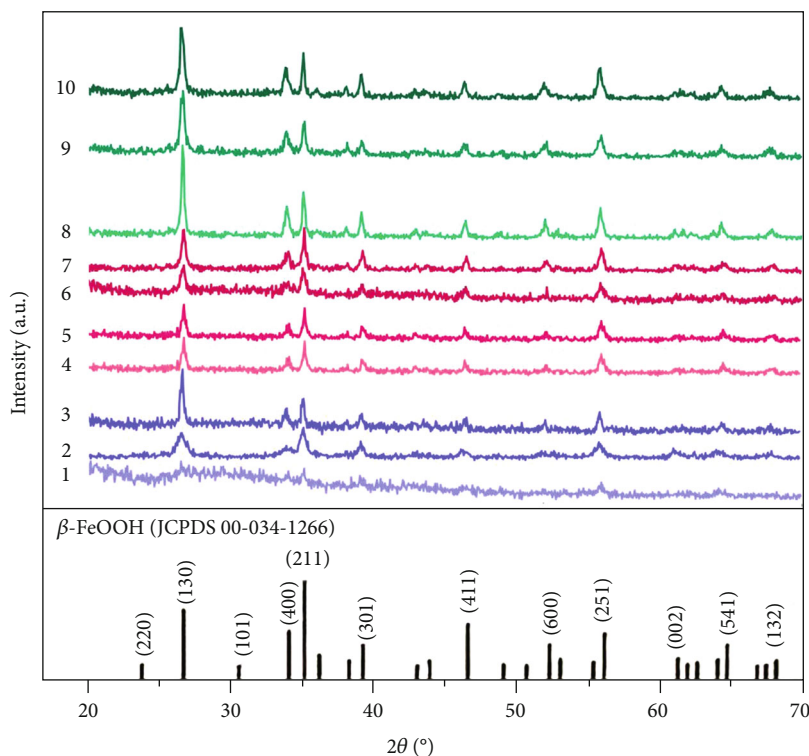


FIGURE 5: XRD patterns of the β -FeOOH nanorods synthesized by various synthesis experiments (1–10) and the standard pattern of akaganeite (β -FeOOH) crystals (JCPDS 00-034-1266).

TABLE 3: Zeta potential values and ICP-OES analysis results of β -FeOOH nanorods obtained from synthetic Exp. 1-10, with and without the presence of surfactants.

Experiment	Surfactants (w/v)	Zeta potential (mV)	Charge	Final content ($\mu\text{g/mL}$)
1	—	$-5.21.4 \pm 1.4$	Negative	307.38
2	—	-14.1 ± 2.2	Negative	278.38
3	—	-21.2 ± 2.3	Negative	212.68
4	PEG-1%	-27.4 ± 2.0	Negative	242.02
5	PEG-3%	-41.3 ± 0.3	Negative	240.89
6	PEG-3%	-45.3 ± 0.5	Negative	286.84
7	PEG-6%	-54.2 ± 0.4	Negative	235.67
8	PEI-0.25%	15.5 ± 5.8	Positive	257.845
9	PEI-0.5%	56.3 ± 0.2	Positive	270.65
10	PEI-1.25%	62.9 ± 0.6	Positive	252.54

presence PEI in the synthesis process contributed to achieving NRs with remarkably higher potential of antimicrobial activities: Exp. 8 > Exp. 6 > Exp. 1. PEG and PEI are synthetic polymers considered individually antimicrobial agents and act as microbicidal enhancers in antibiotics, especially against resistant bacterial species [52, 53]. Coating of polycationic polymers such as PEI exhibited highly electrostatically interact with the bacterial membrane due to its negatively charged

and result in increased membrane permeability, penetration of conjugated materials to bacteria cells, and finally disturbing cell structure and raising cell death [53]. Grafted PEG coating was also found to be contributed to the bactericidal effects of nanocomposites, particularly against resistant bacteria species, by providing a hydrophilic environment to avoid bacterial inhesion and biofilm formation, which also gives the conjugated nanomaterials offer additional bactericidal effects [54]. Thus, the higher antibacterial action of PEG and PEI conjugated synthesized NRs could be assigned to polymers' instint antimicrobial properties as well as synergistic effects of these polymers.

On the other hand, the impact of aspect ratio on the antibacterial efficacy of NRs cannot be ignored. The aspect ratio is considered a critical factor in the cellular uptake of rod-like NPs [55]. NP uptake by microorganisms is related to physicochemical properties, particle orientation, and membrane properties. Moreover, the surface active agents can be involved in particle characterization changes such as aspect ratio and interactions with biological samples, membrane wrapping, and subsequent internalization [56]. The higher aspect ratio of NRs is less favored for microbial particle uptake and antimicrobial efficacy.

In the present case, Exp. 1, 6, and 8 displayed the aspect ratios of 3.676, 3.58, and 1.409, respectively. Exp. 8 obtained a lower aspect ratio due to different synthesis conditions and the presence of PEI. Based on the results, these samples exhibited remarkably more antimicrobial impacts on all microbial species, which along with PEI antimicrobial activities; it could be related to the decreased aspect ratio of these

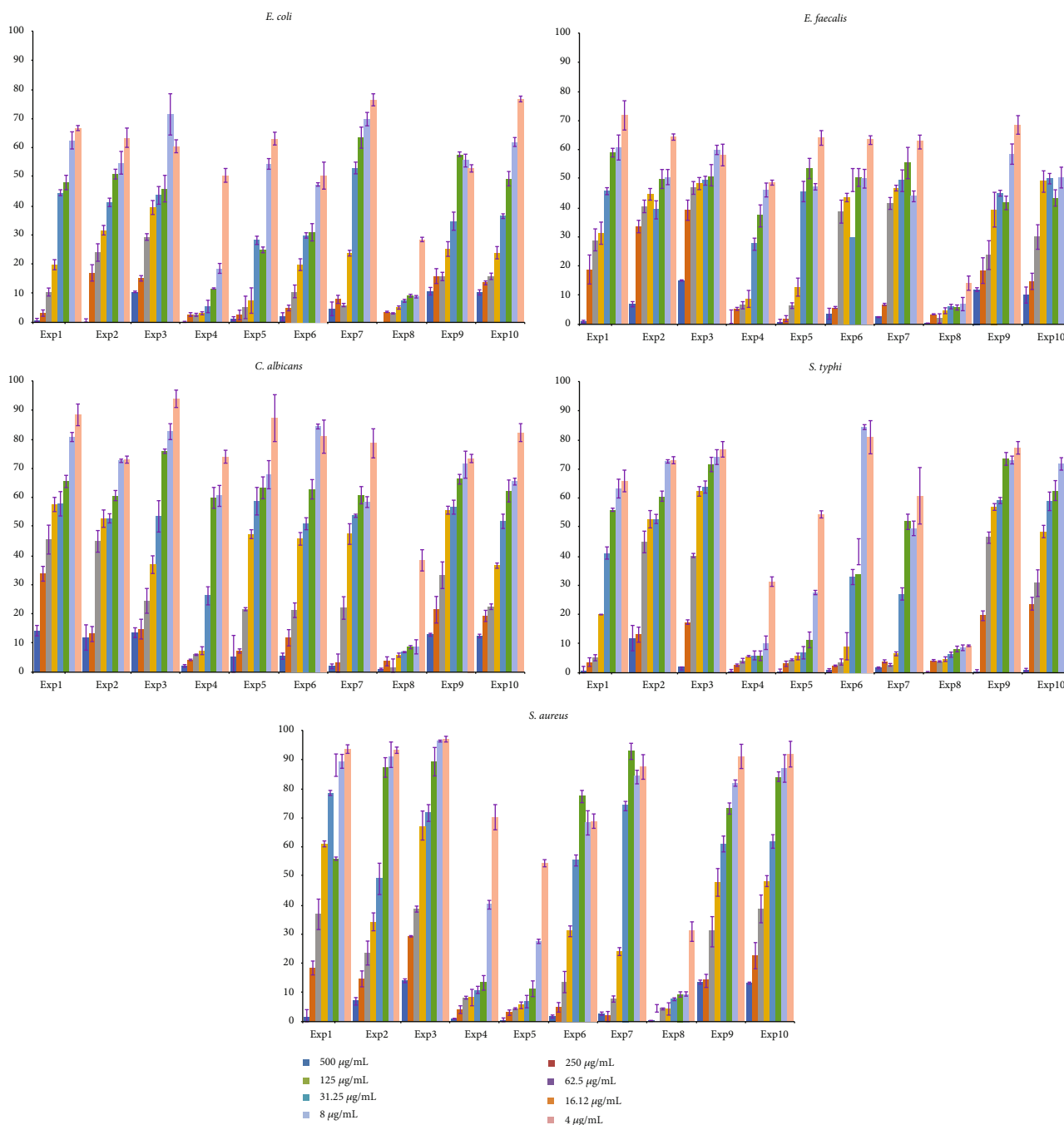


FIGURE 6: Viability percentage of five tested microorganism species, *E.coli*, *S. typhi*, *E. faecalis*, *S. aureus*, and *C. albicans*, treated by various concentrations of each as-prepared β -FeOOH nanorod based on the designed experiments (1–10).

samples (Figure 6). Our experiments were consistent with previous results of NR antimicrobial analysis. Ojha et al. reported that the lower aspect ratio of silver NRs exhibited significantly further antibacterial efficiency against both Gram-positive and Gram-negative bacterial species, comparing the aspect ratio of 1.8 and 3 [57].

More in detail, although the NRs obtained from Exp. 9 and 10 were synthesized in the presence of surfactant PEI, almost no antimicrobial effects of tested microorganisms with MIC $\geq 500 \mu\text{g/mL}$ in all species were shown. It could be related to the larger size of NPs, which is a determining

factor in the biological activities of nanomaterials. NRs synthesized in the presence of PEG (Exp. 4-7) provided an appropriately moderate susceptibility in all tested microbial species because of almost moderate particle size among synthesized NRs and appropriate aspect ratios, about 3-3.6.

C. albicans exhibited the least susceptibility to NRs with generally the most MIC value among all tested microbial species (Table 4). *C. albicans* is one of the opportunistic and pathogenic fungal species posing a particular challenge to the healthcare system due to their increasing drug resistance that should be addressed preferably [58]. Exp. 4

TABLE 4: MIC value of microbial strains treated with β -FeOOH nanorods obtained from the designed synthetic experiments, with and without the presence of surfactants.

Experiment	Surfactants (w/v)	<i>S. typhi</i> ($\mu\text{g/mL}$)	<i>E. coli</i> ($\mu\text{g/mL}$)	<i>E. faecalis</i> ($\mu\text{g/mL}$)	<i>S. aureus</i> ($\mu\text{g/mL}$)	<i>C. albicans</i> ($\mu\text{g/mL}$)
1	—	125	250	500	500	>500
2	—	250	500	500	500	>500
3	—	500	>500	>500	>500	>500
4	PEG-1%	16.12	31.25	62.5	62.5	62.5
5	PEG-3%	31.25	62.5	125	125	250
6	PEG-3%	62.5	250	250	250	500
7	PEG-6%	62.5	125	250	125	250
8	PEI-0.25%	4	8	8	8	8
9	PEI-0.5%	500	>500	>500	>500	>500
10	PEI-1.25%	500	>500	500	>500	>500

(PEG: 1% w/v , aspect ratio: 2.919) and Exp. 8 (PEI: 0.25% w/v , aspect ratio: 1.409) displayed high antifungal potentials with MIC values of 62.5 and 8 $\mu\text{g/mL}$, respectively, which could be considered as an antifungal agent in this case.

4. Conclusion

FeOOH NRs, especially in the β -phase, have attracted much attention in recent years to apply in biomedical applications. With the ever-increasing challenge of antimicrobial resistance, new innovative strategies are in high demand to combat. In the current study, ten synthesis experiments of β -FeOOH NRs are designed to optimize the NRs' properties toward the desirable antimicrobial potential. Reaction conditions, including reaction time and temperature and concentration of iron salt precursors, were considered essential in final particle characteristics and biological activities. Although these factors could affect particle size and aspect ratio, ferric ion concentration showed a dominant effect on the morphology of NRs. NRs also synthesized with and without the presence of surfactants of PEG and PEI, which could play good controlling roles in the size and growth pattern of NP crystals. The aspect ratio was also independent of all factors except ferric ion concentrations.

To sum up, our work indicated that synthetic conditions and the kind and concentration of surfactants contribute to the characterization properties and biological activities of final β -FeOOH NRs. Moreover, β -FeOOH NRs synthesized in the presence of surfactants exhibited more antimicrobial activities against Gram-positive and Gram-negative bacteria and fungi species, even though Gram-negative bacteria showed more susceptibility against NRs. Also, NRs synthesized in the presence of PEG generally revealed relatively moderate antimicrobial effects against tested bacterial and fungal species of final synthesized NPs compared to high antimicrobial activities of PEI surfactant. As mentioned above, surface active agents, particle size, and particularly aspect ratio are crucial decisive factors in the biological activities of β -FeOOH NRs as well as the concentration of NRs. Though further experimental investigations are required, the decent biocompatibility and antimicrobial effi-

cacy of β -FeOOH NPs make them promising candidates for various biomedical applications.

Data Availability

All data used to support the findings of this study are included within the article.

Conflicts of Interest

The authors declare that there is no conflict of interest regarding the publication of this paper.

Authors' Contributions

Fatemeh Mohammadi and Salme Amiri contributed equally to this work.

Acknowledgments

This work was supported by the Shiraz University of Medical Sciences (grant number 25684).

References

- [1] *10 global health issues to track in 2021*, World Health Organization, 2020, <https://www.who.int/news-room/spotlight/10-global-health-issues-to-track-in-2021>.
- [2] N. E. Eleraky, A. Allam, S. B. Hassan, and M. M. Omar, "Nanomedicine fight against antibacterial resistance: an overview of the recent pharmaceutical innovations," *Pharmaceutics*, vol. 12, no. 2, p. 142, 2020.
- [3] F. Fatima, S. Siddiqui, and W. A. Khan, "Nanoparticles as novel emerging therapeutic antibacterial agents in the antibiotics resistant era," *Biological Trace Element Research*, vol. 199, no. 7, pp. 2552–2564, 2021.
- [4] S. Kumar, S. P. Pawar, K. Chatterjee, and S. Bose, "Antimicrobial and conducting polymer substrate derived from hybrid structures of silver nanoparticles and multiwall carbon nanotubes," *Materials Technology*, vol. 29, Supplement 1, pp. B59–B63, 2014.
- [5] V. Agarwal and K. Chatterjee, "Recent advances in the field of transition metal dichalcogenides for biomedical applications," *Nanoscale*, vol. 10, no. 35, pp. 16365–16397, 2018.

- [6] P. K. Samantaray, S. Indrakumar, K. Chatterjee, V. Agarwal, and S. Bose, "'Template-free' hierarchical MoS₂ foam as a sustainable 'green' scavenger of heavy metals and bacteria in point of use water purification," *Nanoscale Advances*, vol. 2, no. 7, pp. 2824–2834, 2020.
- [7] F. Mohammadi, A. Gholami, N. Omidifar, A. Amini, S. Kianpour, and S.-M. Taghizadeh, "The potential of surface nano-engineering in characteristics of cobalt-based nanoparticles and biointerface interaction with prokaryotic and human cells," *Colloids and Surfaces. B, Biointerfaces*, vol. 215, p. 112485, 2022.
- [8] S. M. Mousavi, S. A. Hashemi, A. Gholami et al., "Bioinorganic synthesis of polyrhodanine stabilized Fe₃O₄/graphene oxide in microbial supernatant media for anticancer and antibacterial applications," *Bioinorganic Chemistry and Applications*, vol. 2021, Article ID 9972664, 12 pages, 2021.
- [9] S. R.-A. Narjes Ebrahimi, A. Ebrahiminezhad, Y. Ghasemi, A. Gholami, and H. Seradj, "Comparative study on characteristics and cytotoxicity of bifunctional magnetic-silver nanostructures: synthesized using three different reducing agents," *Acta Metallurgica Sinica*, vol. 29, no. 4, pp. 326–334, 2016.
- [10] A. Gholami, S. Rasoul-amini, A. Ebrahiminezhad, S. H. Seradj, and Y. Ghasemi, "Lipoamino acid coated superparamagnetic iron oxide nanoparticles concentration and time dependently enhanced growth of human hepatocarcinoma cell line (Hep-G2)," *Journal of Nanomaterials*, vol. 2015, Article ID 451405, 9 pages, 2015.
- [11] S. A. Hashemi, S. M. Mousavi, S. Bahrani et al., "Bio-enhanced polyrhodanine/graphene oxide/Fe₃O₄ nanocomposite with kombucha solvent supernatant as ultra-sensitive biosensor for detection of doxorubicin hydrochloride in biological fluids," *Materials Chemistry and Physics*, vol. 279, p. 125743, 2022.
- [12] A. Gholami, S. M. Mousavi, S. A. Hashemi, Y. Ghasemi, W. H. Chiang, and N. Parvin, "Current trends in chemical modifications of magnetic nanoparticles for targeted drug delivery in cancer chemotherapy," *Drug Metabolism Reviews*, vol. 52, no. 1, pp. 205–224, 2020.
- [13] S. M. Dadfar, D. Camozzi, M. Darguzyte et al., "Size-isolation of superparamagnetic iron oxide nanoparticles improves MRI, MPI and hyperthermia performance," *Journal of nanobiotechnology*, vol. 18, no. 1, p. 22, 2020.
- [14] A. Gholami, F. Mohammadi, Y. Ghasemi, N. Omidifar, and A. Ebrahiminezhad, "Antibacterial activity of SPIONs versus ferrous and ferric ions under aerobic and anaerobic conditions: a preliminary mechanism study," *IET Nanobiotechnology*, vol. 14, no. 2, pp. 155–160, 2020.
- [15] Z. Huang, F. Han, M. Li, Z. Zhou, X. Guan, and L. Guo, "Which phase of iron oxyhydroxides (FeOOH) is more competent in overall water splitting as a photocatalyst, goethite, akaganeite or lepidocrocite? A DFT-based investigation," *Computational Materials Science*, vol. 169, p. 109110, 2019.
- [16] X. Wang, X. Chen, L. Gao et al., "Synthesis of β -FeOOH and α -Fe₂O₃ nanorods and electrochemical properties of β -FeOOH," *Journal of Materials Chemistry*, vol. 14, no. 5, pp. 905–907, 2004.
- [17] S.-M. Taghizadeh, A. Berenjian, M. Zare, and A. Ebrahiminezhad, "New perspectives on iron-based nanostructures," *Processes*, vol. 8, no. 9, p. 1128, 2020.
- [18] G. Kasparis, A. S. Erdocio, J. M. Tuffnell, and N. T. K. Thanh, "Synthesis of size-tuneable β -FeOOH nanoellipsoids and a study of their morphological and compositional changes by reduction," *CrystEngComm*, vol. 21, no. 8, pp. 1293–1301, 2019.
- [19] H. Cui, L. Wang, M. Shi, and Y. Li, "Morphology and phase control of iron oxide polymorph nanoparticles," *Materials Research Express*, vol. 4, no. 4, article 045006, 2017.
- [20] X. Shi, L. Qin, G. Xu et al., " β -FeOOH: a new anode for potassium-ion batteries," *Chemical Communications*, vol. 56, no. 26, pp. 3713–3716, 2020.
- [21] A. Berenjian, M. Karami-Darehnananji, S.-M. Taghizadeh, E. Mirzaei, R. Heidari, and A. Ebrahiminezhad, "Bio-assisted synthesis of food-grade FeOOH nanoellipsoids as promising iron supplements for food fortification," *Applied Food Biotechnology*, vol. 8, no. 1, pp. 71–77, 2020.
- [22] A. N. Fomenko, O. V. Bakina, S. O. Kazantsev, and A. M. Kondranova, "Synthesis of iron oxide based nanostructures with antimicrobial activity," *IOP Conf Ser Mater Sci Eng*, vol. 447, article 012069, 2018.
- [23] G. Yi, S. P. Teong, S. Liu, S. Chng, Y. Y. Yang, and Y. Zhang, "Iron-based nano-structured surfaces with antimicrobial properties," *Journal of Materials Chemistry B*, vol. 8, no. 44, pp. 10146–10153, 2020.
- [24] D. T. N. Pham, F. Khan, T. T. V. Phan et al., "Biofilm inhibition, modulation of virulence and motility properties by FeOOH nanoparticle in *Pseudomonas aeruginosa*," *Brazilian Journal of Microbiology*, vol. 50, no. 3, pp. 791–805, 2019.
- [25] Y. Wei, R. Ding, C. Zhang et al., "Facile synthesis of self-assembled ultrathin α -FeOOH nanorod/graphene oxide composites for supercapacitors," *Journal of Colloid and Interface Science*, vol. 504, pp. 593–602, 2017.
- [26] Y. Piao, J. Kim, H. B. Na et al., "Wrap-bake-peel process for nanostructural transformation from β -FeOOH nanorods to biocompatible iron oxide nanocapsules," *Nature materials*, vol. 7, no. 3, pp. 242–247, 2008.
- [27] R. M. Cornell and U. Schwertmann, *The Iron Oxides: Structure, Properties, Reactions, Occurrences and Uses*, John Wiley & Sons, 2003.
- [28] M. Karami-Darehnananji, S.-M. Taghizadeh, E. Mirzaei, A. Berenjian, and A. Ebrahiminezhad, "Size tuned synthesis of FeOOH nanorods toward self-assembled nanoarchitectonics," *Langmuir*, vol. 37, no. 1, pp. 115–123, 2021.
- [29] J. Yue, X. Jiang, and A. Yu, "Experimental and theoretical study on the β -FeOOH nanorods: growth and conversion," *Journal of Nanoparticle Research*, vol. 13, no. 9, pp. 3961–3974, 2011.
- [30] F. N. Sayed and V. Polshettiwar, "Facile and sustainable synthesis of shaped iron oxide nanoparticles: effect of iron precursor salts on the shapes of iron oxides," *Scientific Reports*, vol. 5, no. 1, p. 9733, 2015.
- [31] H. Moradpoor, M. Safaei, F. Rezaei et al., "Optimisation of cobalt oxide nanoparticles synthesis as bactericidal agents," *Open access Macedonian journal of medical sciences*, vol. 7, no. 17, pp. 2757–2762, 2019.
- [32] T. Zhu, J. S. Chen, and X. W. Lou, "Glucose-assisted one-pot synthesis of FeOOH nanorods and their transformation to Fe₃O₄@ carbon nanorods for application in lithium ion batteries," *Journal of Physical Chemistry C*, vol. 115, no. 19, pp. 9814–9820, 2011.
- [33] K. Chen, X. Chen, and D. Xue, "Hydrothermal route to crystallization of FeOOH nanorods via FeCl₃·6H₂O: effect of Fe³⁺ concentration on pseudocapacitance of iron-based materials," *CrystEngComm*, vol. 17, no. 9, pp. 1906–1910, 2015.

- [34] X. Wei, X. Mou, Y. Zhou, Y. Li, and W. Shen, "Fabrication of rod-shaped β -FeOOH: the roles of polyethylene glycol and chlorine anion," *Science China Chemistry*, vol. 59, no. 7, pp. 895–902, 2016.
- [35] J. Zhang, X. Zhu, and K. Yu, "Surfactant-assisted nanorod synthesis of α -FeOOH and its adsorption characteristics for methylene blue," *Journal of Materials Research*, vol. 29, no. 4, pp. 509–518, 2014.
- [36] Y. Zhou, W. Wu, G. Hu, H. Wu, and S. Cui, "Hydrothermal synthesis of ZnO nanorod arrays with the addition of polyethyleneimine," *Materials Research Bulletin*, vol. 43, no. 8-9, pp. 2113–2118, 2008.
- [37] J. Mohapatra, A. Mitra, H. Tyagi, D. Bahadur, and M. Aslam, "Iron oxide nanorods as high-performance magnetic resonance imaging contrast agents," *Nanoscale*, vol. 7, no. 20, pp. 9174–9184, 2015.
- [38] R. Parameshwari, P. Priyadarshini, and G. Chandrasekaran, "Optimization, structural, spectroscopic and magnetic studies on stable akaganeite nanoparticles via co-precipitation method," *American Journal of Materials Science*, vol. 1, no. 1, pp. 18–25, 2011.
- [39] E. Murad and J. L. Bishop, "The infrared spectrum of synthetic akaganéite, β -FeOOH," *American Mineralogist*, vol. 85, no. 5-6, pp. 716–721, 2000.
- [40] S. M. Pasini, M. A. Batistella, S. M. A. G. U. de Souza, J. Wang, D. Hotza, and A. A. U. de Souza, "Thermal degradation and flammability of TiO₂-polyetherimide nanocomposite fibers," *Polymer Bulletin*, vol. 77, no. 9, pp. 4937–4958, 2020.
- [41] S. Arabi, H. Akbari Javar, and M. Khoobi, "Preparation and characterization of modified polyethyleneimine magnetic nanoparticles for cancer drug delivery," *Journal of Nanomaterials*, vol. 2016, Article ID 2806407, 6 pages, 2016.
- [42] S. K. Seol, D. Kim, S. Jung, W. S. Chang, and J. T. Kim, "One-step synthesis of PEG-coated gold nanoparticles by rapid microwave heating," *Journal of Nanomaterials*, vol. 2013, Article ID 531760, 6 pages, 2013.
- [43] J. Charmi, H. Nosrati, J. Mostafavi Amjad, R. Mohammadkhani, and H. Danafar, "Polyethylene glycol (PEG) decorated graphene oxide nanosheets for controlled release curcumin delivery," *Helvion*, vol. 5, no. 4, article e01466, 2019.
- [44] H. Ahmad, K. Umar, S. Ali, P. Singh, S. Islam, and H. Khan, "Pre-concentration and speciation of arsenic by using a graphene oxide nanoconstruct functionalized with a hyperbranched polyethyleneimine," *Mikrochimica Acta*, vol. 185, no. 6, 2018.
- [45] R. Wang, L. Wu, D. Zhuo, Z. Wang, and T. Y. Tsai, "Fabrication of fullerene anchored reduced graphene oxide hybrids and their synergistic reinforcement on the flame retardancy of epoxy resin," *Nanoscale Research Letters*, vol. 13, no. 1, p. 351, 2018.
- [46] K. Grenda, A. Idström, L. Evenäs, M. Persson, K. Holmberg, and R. Bordes, "An analytical approach to elucidate the architecture of polyethyleneimines," *Journal of Applied Polymer Science*, vol. 139, no. 7, p. 51657, 2022.
- [47] X. Zhang, L. An, J. Yin, P. Xi, Z. Zheng, and Y. Du, "Effective construction of high-quality iron oxy-hydroxides and Co-doped iron oxy-hydroxides nanostructures: towards the promising oxygen evolution reaction application," *Scientific Reports*, vol. 7, no. 1, pp. 1–10, 2017.
- [48] N. K. Chaudhari and J.-S. Yu, "Size control synthesis of uniform β -FeOOH to high coercive field porous magnetic α -Fe₂O₃ nanorods," *Journal of Physical Chemistry C*, vol. 112, no. 50, pp. 19957–19962, 2008.
- [49] M. Nabavizadeh, A. Abbaszadegan, A. Gholami et al., "Anti-biofilm efficacy of positively charged imidazolium-based silver nanoparticles in *Enterococcus faecalis* using quantitative real-time PCR," *Jundishapur Journal of Microbiology*, vol. 10, no. 10, article e55616, 2017.
- [50] A. Abbaszadegan, M. Nabavizadeh, A. Gholami et al., "Positively charged imidazolium-based ionic liquid-protected silver nanoparticles: a promising disinfectant in root canal treatment," *International Endodontic Journal*, vol. 48, no. 8, pp. 790–800, 2015.
- [51] F. D. Lowy, "Antimicrobial resistance: the example of *Staphylococcus aureus*," *The Journal of Clinical Investigation*, vol. 111, no. 9, pp. 1265–1273, 2003.
- [52] L. Peng, L. Chang, X. Liu et al., "Antibacterial property of a polyethylene glycol-grafted dental material," *ACS Applied Materials & Interfaces*, vol. 9, no. 21, pp. 17688–17692, 2017.
- [53] W. Akhtar, M. Shoaib, I. M. Khan et al., "Improved bactericidal activity of polyethyleneimine grafted graphene oxide nanocomposite against *Staphylococcus aureus* and *Escherichia coli*," *Biomedical Journal of Scientific & Technical Research*, vol. 27, no. 2, pp. 20616–20624, 2020.
- [54] H. Shi, H. Liu, S. Luan et al., "Effect of polyethylene glycol on the antibacterial properties of polyurethane/carbon nanotube electrospun nanofibers," *RSC Advances*, vol. 6, no. 23, pp. 19238–19244, 2016.
- [55] D. Kilinc, C. L. Dennis, and G. U. Lee, "Bio-Nano-magnetic materials for localized mechanochemical stimulation of cell growth and death," *Advanced Materials*, vol. 28, no. 27, pp. 5672–5680, 2016.
- [56] S. Dasgupta, T. Auth, and G. Gompper, "Shape and orientation matter for the cellular uptake of nonspherical particles," *Nano Letters*, vol. 14, no. 2, pp. 687–693, 2014.
- [57] A. K. Ojha, S. Forster, S. Kumar, S. Vats, S. Negi, and I. Fischer, "Synthesis of well-dispersed silver nanorods of different aspect ratios and their antimicrobial properties against gram positive and negative bacterial strains," *Journal of nanobiotechnology*, vol. 11, no. 1, p. 42, 2013.
- [58] H. A. P. Castillo, L. N. M. Castellanos, R. M. Chamorro, R. R. Martínez, and E. O. Borunda, *Nanoparticles as New Therapeutic Agents against Candida albicans*, *Candida Albicans*, Doblín Sandai, IntechOpen, 2018.

Research Article

Optimized Synthesis of Xanthan gum/ZnO/TiO₂ Nanocomposite with High Antifungal Activity against Pathogenic *Candida albicans*

Fatemeh Ghorbani ¹, Pourya Gorji ¹, Mohammad Salmani Mobarakeh ²,
Hamid Reza Mozaffari ³, Reza Masaeli ⁴, and Mohsen Safaei ^{2,5}

¹Students Research Committee, Kermanshah University of Medical Sciences, Kermanshah, Iran

²Advanced Dental Sciences Research Center, Kermanshah University of Medical Sciences, Kermanshah, Iran

³Department of Oral and Maxillofacial Medicine, School of Dentistry, Kermanshah University of Medical Sciences, Kermanshah, Iran

⁴Department of Dental Biomaterials, School of Dentistry, Tehran University of Medical Sciences, Tehran, Iran

⁵Division of Dental Biomaterials, School of Dentistry, Kermanshah University of Medical Sciences, Kermanshah, Iran

Correspondence should be addressed to Mohsen Safaei; mohsen_safaei@yahoo.com

Received 20 November 2021; Revised 5 March 2022; Accepted 30 March 2022; Published 25 April 2022

Academic Editor: Seyed alireza Hashemi

Copyright © 2022 Fatemeh Ghorbani et al. This is an open access article distributed under the Creative Commons Attribution License, which permits unrestricted use, distribution, and reproduction in any medium, provided the original work is properly cited.

Increased resistance of fungal pathogens to common antimicrobial agents is known as one of the most important human problems. Due to the limited variety of antifungal drugs available, the identification and use of new antifungal drugs are essential. This study aimed to determine the optimal conditions for synthesizing a novel nanocomposite of xanthan gum/ZnO/TiO₂ with the highest antifungal activity against *Candida albicans* (*C. albicans*). For this purpose, nine experiments were designed using the Taguchi method. In the designed experiments, three factors of xanthan gum, ZnO, and TiO₂ nanoparticles have been investigated at three different levels, and the best ratio with the highest antifungal activity was determined. The results showed that in the presence of the synthesized nanocomposite in experiment 3 (xanthan gum 0.01 M, ZnO 0.09 M, and TiO₂ 0.09 M), the inhibition of fungal growth reached 92.51%. The properties of the synthesized nanocomposite and its components were investigated using different characterization methods, which confirmed the formation of nanocomposites with desirable properties. The antifungal activity results showed that the synthesized nanocomposite as an antifungal agent has an effective performance and can be used well in various fields.

1. Introduction

The dramatic increase in microbial resistance to antimicrobials has become a pervasive challenge and a serious threat to public health worldwide. *C. albicans* is one of the most common fungal pathogens in humans. The widespread use of a limited number of antifungal agents has led to drug resistance in treating *C. albicans* infections, a problem that is becoming increasingly important [1]. The range of human infections caused by the *C. albicans* yeast and several related species is significant. They cause various infection levels, from relatively trivial conditions such as oral candidiasis

and genital infections to fatal and systemic infections in patients who have already had serious illnesses. There has been great interest in fighting *Candida* infections, especially *C. albicans*, as fatal infections have become more common and new disorders have been identified with *Candida* [2].

Antifungal drugs often belong to two groups of polyenes and azoles. These compounds act on fungal cells by disrupting the metabolism of RNA or DNA and causing intracellular accumulation of peroxide. The currently available antifungal agents used topically and systemically to treat *C. Albicans* have shown serious side effects that have greatly limited their use. Toxicity and drug resistance are the main

reasons for extensive research on new antifungal compounds [3]. Since discovering and using a new class of antimicrobial compounds is very time-consuming, expensive, and usually unsuccessful, an alternative is to use modern science and design and synthesize compounds with antimicrobial properties. Nanotechnology has solved many current problems by using structures with at least one dimension of 1 to 100 nanometers [4–6]. In recent years, significant studies have been conducted in applications of nanomaterials, and their effectiveness has been observed in many fields. Metal oxides with antimicrobial properties are among the most widely used compounds in various fields [6, 7]. The use of nanomaterials can be effective in combating fungal infections. Due to their special properties, such as proper penetration into target cells and tissues, these particles have been able to provide more inhibitory power with lower concentrations compared to conventional compounds [8].

Extensive sources of zinc metal, reasonable price, antimicrobial, antioxidant, and anticancer properties make zinc a valuable metal as a raw material in the production of various compounds such as mouthwashes and toothpaste that reduce plaque and bad breath [9, 10]. ZnO nanoparticles have successfully inhibited pathogenic microbes such as *Streptococcus mutans* and *Staphylococcus aureus* [11].

Titanium dioxide (TiO_2) has unique properties such as high photocatalytic activity, anticancer, antimicrobial properties, biocompatibility, reactivity, cheap and safe production, nontoxicity, temperature stability, and chemical stability [12, 13]. These properties of TiO_2 are used in the production of food, pharmaceutical, biomedicine, environment, cosmetics, air purification, water disinfection, solar cell production, and antimicrobial compounds [14]. It is an optical catalyst whose antimicrobial applications have been investigated more than any other material with this property [15]. TiO_2 NPs can inactivate microorganisms and exhibit antimicrobial properties by producing hydroxyl free radicals and superoxide [16, 17].

Similar properties are found in natural materials. Xanthan gum is a type of polysaccharide that is naturally produced by the *Xanthomonas* bacterium [18]. Its main chain consists of β -D-glucose units interconnected in positions 1 and 4; in addition, two mannose and glucuronic acid are also involved in its structure [19]. Among the desirable properties of xanthan are nontoxic, inexpensive, with high biocompatibility, thermal stability, resistance to acid and base, high stability and solubility in water, and antimicrobial properties [20, 21].

Due to the tendency of nanoparticles to agglomerate, which leads to the loss of their desirable properties, it is necessary to use strategies to prevent this. The use of nanoparticles in the form of nanocomposites can largely prevent them from agglomerating. For this purpose, this study was designed and conducted for the first time to determine the optimal conditions for the synthesis of xanthan gum/ZnO/ TiO_2 with the highest antifungal properties.

2. Materials and Methods

2.1. TiO_2 Nanoparticle Synthesis. To prepare TiO_2 NPs using the sol-gel method, 10 ml of isopropanol was combined with

10 ml of deionized water, and 20 ml of titanium isopropoxide solution was added dropwise with continuous stirring. The resulting solution was placed at 60 °C for 60 min, the yellow gel formed in the oven was dried at 80 °C, and the gel powder was calcined in air for 3 h at 650 °C [22].

2.2. ZnO Nanoparticle Synthesis. Zinc acetate ($\text{Zn}(\text{CH}_3\text{CO}_2)_2 \cdot 2\text{H}_2\text{O}$) and sodium hydroxide (NaOH) were used to prepare ZnO nanoparticles. First, 0.1 M zinc acetate and 0.2 M sodium hydroxide solutions were prepared by dissolving them in deionized water.

Then two solutions were poured into a beaker and stir at 750 rpm for 2 h at 60 °C. After 2 h, a clear milky white solution was formed. The next step was centrifugation at 5000 rpm for 5 min to precipitate a white product. The precipitate was washed first with deionized water and then with acetone. ZnO NPs were obtained in powder form by drying the product using an oven at 75 °C for 6 h [23].

2.3. Xanthan Gum/ZnO/ TiO_2 Nanocomposite Synthesis. To determine the optimal conditions for the synthesis of xanthan gum/ZnO/ TiO_2 nanocomposite with the highest antimicrobial activity, using Qulitek-4 software according to the Taguchi method, 9 experiments containing different ratios of xanthan gum, ZnO, and titanium NPs were designed. To evaluate the antimicrobial activity of synthesized nanocomposites, using in situ method and 0.01, 0.02, and 0.03 M levels of xanthan gum and 0.03, 0.06, and 0.09 M levels of ZnO and TiO_2 NPs, nine samples of nanocomposites were tested. To synthesize the studied nanocomposite, xanthan gum was prepared commercially; ZnO and TiO_2 NPs were prepared by coprecipitation and sol-gel methods, respectively. In the synthesis of nanocomposites, first, the solutions of the components were stirred separately by a magnetic stirrer for one h. All three solutions were then dispersed at room temperature for 15 min using an ultrasonic homogenizer. Finally, solutions of ZnO and TiO_2 NPs were added simultaneously and dropwise to the solution containing xanthan gum. The final solutions were stirred for one h and then dispersed for 15 min by an ultrasonic homogenizer. Finally, the prepared solution was placed in an oven at 60 °C for 24 h to form nanocomposite sediments. The resulting precipitate was separated from the container with a spatula and ground in a mortar to prepare the final nanocomposite powder [24].

2.4. Antifungal Activity. The antifungal activity of synthesized xanthan gum/ZnO/ TiO_2 nanocomposites on *C. albicans* (ATCC 10231) was studied using the colony forming unit (CFU) method. For this purpose, *C. albicans* was incubated on a Sabouraud dextrose agar (SDA) medium for 48 h at 37 °C to prepare an isolated colony. After that, a colony was taken and dissolved in twice distilled water to obtain an approximate 10^6 CFU/ml concentration. To evaluate the antifungal activity of the synthesized nanocomposites, solutions containing SDA and 9 synthesized nanocomposites (1 mg/ml) were prepared. The resulting solutions were poured into the Petri dish, and after freezing the culture medium, 100 μL of the fungal suspension prepared on the

TABLE 1: Taguchi design of experiments and fungal growth inhibition rate of xanthan/ZnO/TiO₂ synthesized nanocomposite.

Experiment	Xanthan gum (M)			ZnO (M)			TiO ₂ (M)		Fungal growth inhibition (%)	
	0.01	0.02	0.03	0.03	0.06	0.09	0.03	0.06		0.09
1		0.01			0.03			0.03		61.73
2		0.01			0.06			0.06		84.11
3		0.01			0.09			0.09		92.51
4		0.02			0.03			0.06		75.64
5		0.02			0.06			0.09		88.32
6		0.02			0.09			0.03		81.17
7		0.03			0.03			0.09		72.98
8		0.03			0.06			0.03		69.44
9		0.03			0.09			0.06		90.47

TABLE 2: The main effects of different levels of xanthan gum, ZnO, and TiO₂ on growth inhibition of *Candida albicans*.

Factors	Level 1	Level 2	Level 3
Xanthan gum	79.45	81.71	77.63
ZnO	70.12	80.62	88.05
TiO ₂	70.78	83.41	84.60

TABLE 3: The interactions effects of studied factors on growth inhibiting of *Candida albicans*.

Interacting factor pairs	Column	Severity index (%)	Optimum conditions
Xanthan gum × TiO ₂	1 × 3	45.33	[1,3]
Xanthan gum × ZnO	1 × 2	15.75	[1,3]
ZnO × TiO ₂	2 × 3	1.23	[3,3]

culture medium was completely cultured using a swap. In the control group, 100 μ L of fungal suspension was cultured on a pure SDA medium. The number of colonies was counted for 9 experimental and control groups after 96 h of incubation at 28 °C. The inhibition of fungal growth by each of the synthesized nanocomposites is calculated using the following equation:

$$\text{Growth fungus inhibition rate (\%)} = \frac{C_g - E_g}{C_g} \times 100, \quad (1)$$

where C_g is the average growth of colonies in the control group and E_g is the average growth in the experimental group. Thus, the optimal conditions for synthesizing nanocomposites with the highest antifungal activity were determined from 9 experiments. All experiments were repeated three times.

2.5. Characterization. The properties of the synthesized nanocomposite and its components were investigated using different characterization methods, including Fourier transforms infrared (FTIR) spectroscopy (Thermo Company at RT, USA), X-ray diffraction (XRD) (Philips X'Pert (40 kV,

TABLE 4: The analysis of variance of factors affecting the growth inhibition of *Candida albicans*.

Factors	DOF	Sum of squares	Variance	F ratio (F)	Pure sum	Percent (%)
Xanthan gum	2	25.07	12.53	15.93	23.49	2.71
ZnO	2	487.15	243.57	309.61	485.57	56.09
TiO ₂	2	351.95	175.97	223.68	350.38	40.47

DOF, degree of freedom.

TABLE 5: The optimum conditions for the synthesis of xanthan/ZnO/TiO₂ nanocomposite with the highest antifungal activity.

Factors	Level	Contribution
Xanthan gum	2	2.11
ZnO	3	8.45
TiO ₂	3	5.01
Total contribution from all factors		15.57
Current grand average of performance		79.60
Fungal growth inhibition at optimum condition		95.17

30 mA), The Netherlands), field emission scanning electron microscope (FESEM) (TESCAN Company, MIRA III model, Czech Republic), SAMX detector (France) on FESEM, transmission electron microscope (TEM) (TEM Philips EM208S, The Netherlands), ultraviolet-visible (UV-Vis) spectroscopy (Shimadzu Company UV-160 A model, Japan), and thermal analysis (TGA-DTA) (TA Company, Q600 model).

3. Results and Discussion

3.1. Antifungal Activity. Optimal conditions for the production of xanthan gum/ZnO/TiO₂ nanocomposites with the highest antifungal activity were determined based on 9 experiments designed by the Taguchi method. Table 1 shows the effect of nanocomposites synthesized under different conditions on the growth inhibition of *C. albicans*. The results showed that the nanocomposites produced in

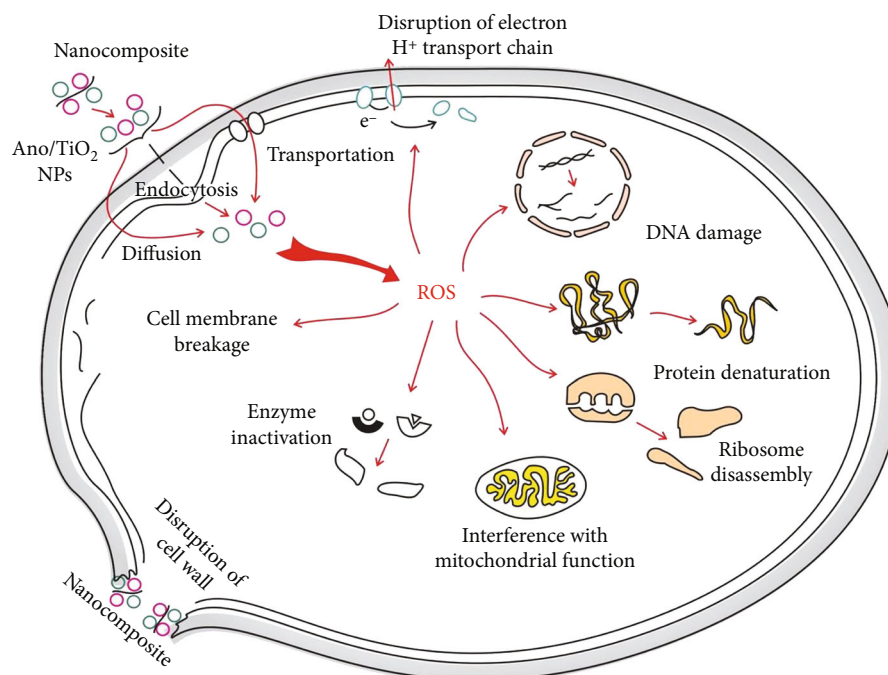


FIGURE 1: Schematic mechanisms for antifungal activity of xanthan gum/ZnO/TiO₂ nanocomposite.

experiment 3 (xanthan gum 0.01 M, ZnO NPs 0.09 M, and TiO₂NPs 0.09 M) had the highest antifungal activity against *C. albicans* and, under those conditions, the highest inhibition of fungal growth (92.51%) occurred.

Table 2 shows the effect of xanthan gum, ZnO, and TiO₂NPs factors on the growth inhibition of *C. albicans*. The results indicate that the xanthan gum factor at level 2 and ZnO and TiO₂ NPs at level 3 had the greatest effect in inhibiting the growth of *C. albicans*.

The interaction of factors on the growth inhibition of *C. albicans* is presented in Table 3. Xanthan gum in the first level and TiO₂ in the third level had the most interaction and the growth inhibition of *C. albicans* at 45.33%. Xanthan gum in the first level and ZnO in the third level showed a significant interaction on the growth inhibition of *C. albicans* by 15.75%. The lowest percentage of interaction intensity index belonged to ZnO and TiO₂ in the third level at 1.23%.

The analysis of variance of the parameters affecting the growth inhibition of *C. albicans* is presented in Table 4. The highest effect on inhibiting the growth of *C. albicans* was shown by ZnO with an effect of 56.09%, TiO₂ by 40.47%, and xanthan gum by 2.71%, respectively.

After reviewing the data and analyzing the effect of each factor and their interaction, the optimal conditions for the synthesis of xanthan gum/ZnO/TiO₂ nanocomposite with the highest antifungal activity were estimated (Table 5). Based on these results, ZnO had the highest contribution, and xanthan gum had the lowest contribution in inhibiting the growth of *C. albicans*, and TiO₂ showed an effect between these two factors and close to ZnO. The second level was the most appropriate level for the xanthan gum factor and the third level for ZnO and TiO₂NPs factors. Based on the results, it was estimated that the synthesized

nanocomposite in optimal conditions inhibited about 95% of fungal growth, which was most consistent with the results of experiment 3.

Previous similar studies have reported the optimal antimicrobial properties of nanomaterials and their components. Nanoparticles currently used in the clinical field are limited by agglomeration. Many studies have used the modification of impurities and the synthesis of nanocomposites to prevent nanoparticles from agglomerating and disperse nanoparticles in different environments. In other words, the modification in this way is one of the most effective ways to regulate and control the interaction of nanoparticles and germs [25–28].

The larger area and high density of nanoparticles allow them to show antimicrobial activity more favorably on the surface of fungi with more interaction. In addition, nanoparticles combined with polymers or coated on the surfaces of biocompatible materials have been used to improve their antimicrobial properties. The study of the mechanism of antimicrobial activity of nanocomposites containing metal oxides indicates that these nanostructures can cause the destruction of the fungal cell wall and the penetration of nanoparticles into the cell. Nanoparticles that pass through the cell wall are not fully understood. However, their transport, diffusion and endocytosis, and entry into the cell can lead to the production of reactive oxygen species (ROS) and thus interfere with the function of many intracellular organs [29, 30]. Reactive oxygen species seem to play a major role in antifungal activity. By inducing oxidative stress, they can destroy all biomolecules in the cell (including proteins and DNA) and disrupt the function of intracellular organs [31]. Nanostructures can also cause fungal death by damaging cellular enzymes and disrupting the electron transfer chain (Figure 1).

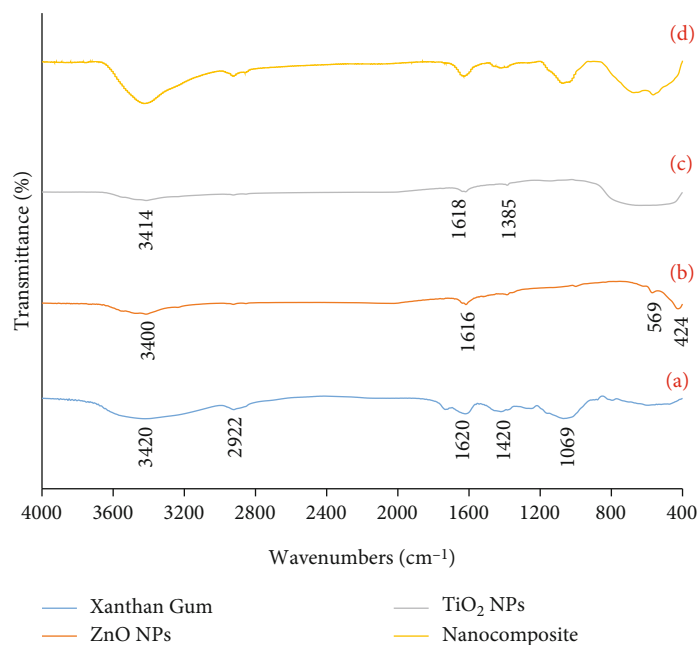


FIGURE 2: FTIR spectra of xanthan gum (a), ZnO NPs (b), TiO₂ NPs (c), and xanthan Gum/ZnO/TiO₂ nanocomposite (d).

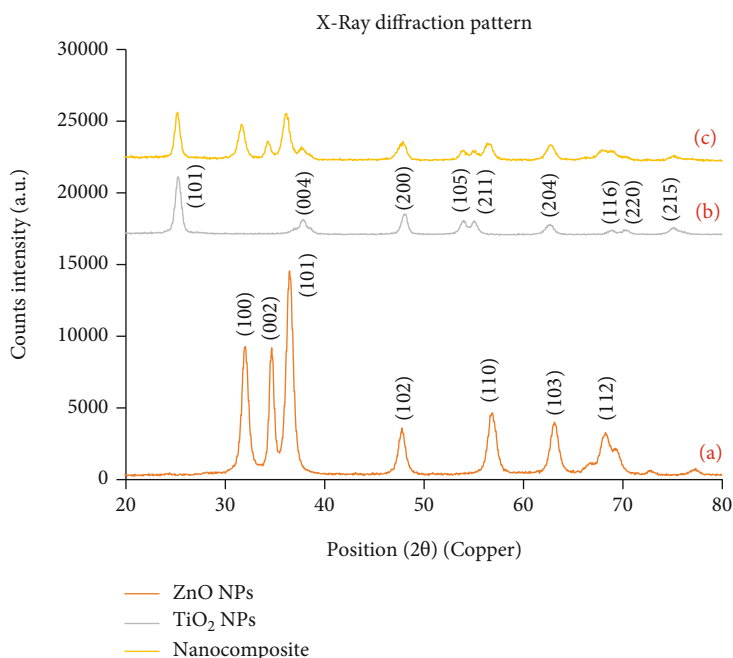


FIGURE 3: XRD Pattern of ZnO NPs (a), TiO₂ NPs (b), and xanthan gum/ZnO/TiO₂ nanocomposite (c).

3.2. FTIR Analysis. The FTIR spectra of xanthan gum (diagram a), ZnO NPs (diagram b), TiO₂ nanoparticles (diagram c), and synthesized nanocomposites (diagram d), in the wavelength range of 400-4000 cm⁻¹, are shown in Figure 2.

In the FTIR spectrum of xanthan gum (diagram a), two peaks at positions 3420 and 2922 cm⁻¹ were observed for the tensile bonds of -OH and -CH, respectively. Asymmetric and symmetric tensile vibrations related to carboxylate group -COO- bonds were shown at 1620 and 1420 cm⁻¹,

respectively. A wide absorption peak was observed at 1069 cm⁻¹ due to the tensile vibration of the glycosidic bond [32].

In the FTIR spectrum of ZnO NPs (diagram b), a wide adsorption peak in the range of 3100-3700 cm⁻¹ was observed for the tensile bonds of O-H due to residual alcohols, water, and Zn-OH bond. The flexural state was shown in the H-OH bond of the ZnO NPs at the 1616 cm⁻¹ position. The strongest wide adsorbed band was observed at

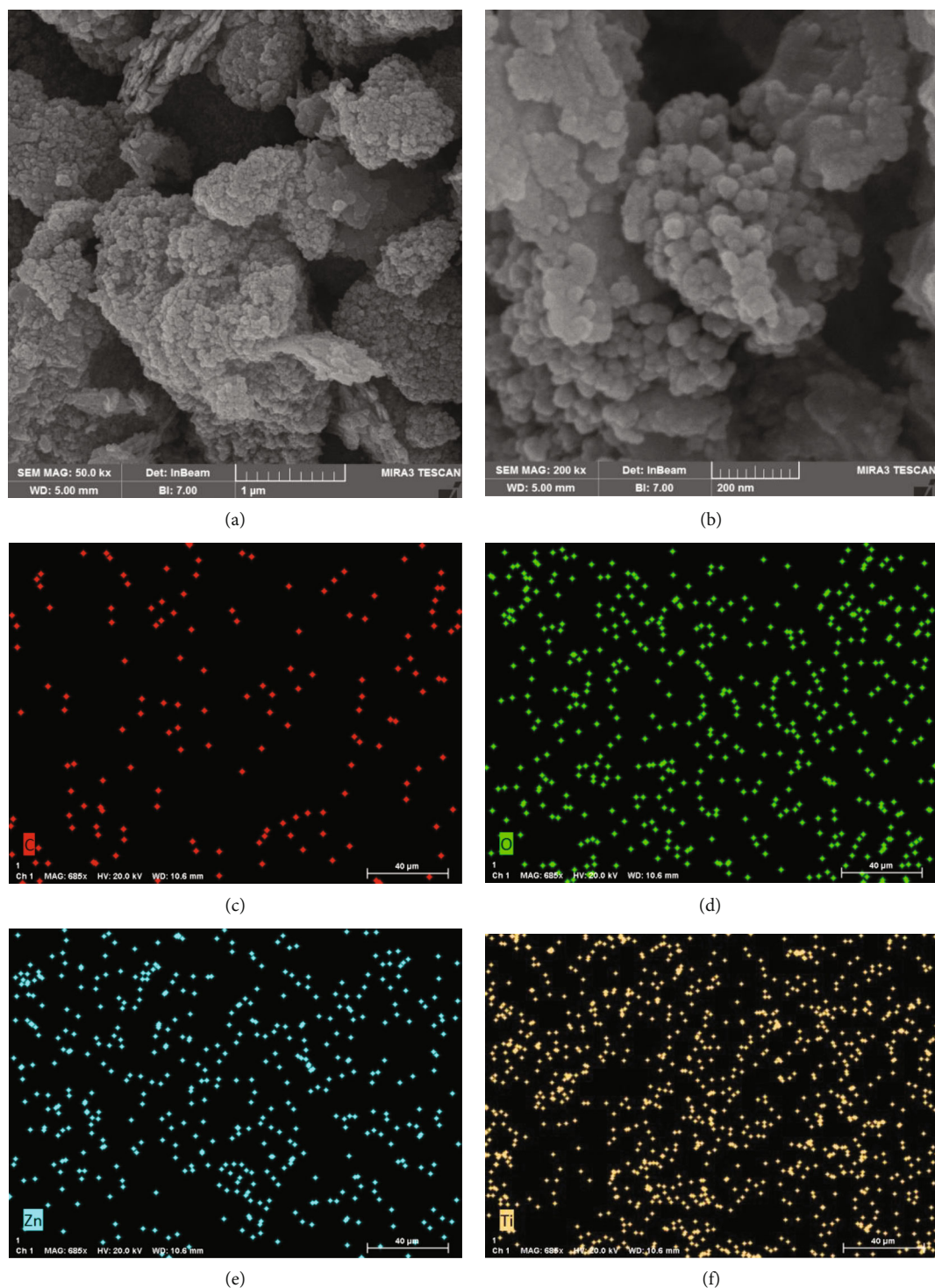


FIGURE 4: The scanning electron microscope images of xanthan gum/ZnO/TiO₂ nanocomposite at different magnification (a, b) and corresponding energy-dispersive X-ray spectroscopy (EDS) elemental mapping for C (c), O (d), Ti (e), and Zn (f).

424 cm⁻¹ due to the tensile vibrations related to oxygen and zinc. Zn-O tensile bands were observed at 424 and 569 cm⁻¹ for pure samples of ZnO NPs [33].

In the FTIR spectrum of TiO₂ nanoparticles (diagram c), the peaks observed at 3414 cm⁻¹ and 1635 cm⁻¹ refer to the adsorbed moisture and the O-H surface groups. The peak

observed in the 1618 cm⁻¹ region corresponds to the bending vibrations of the water molecule, and the peak index of the 1385 cm⁻¹ region is due to the carbonate group, which is created by the adsorption of ambient carbon dioxide by nanoparticles. Sharp peaks observed in the range below 850 cm⁻¹ showed the binding of oxygen to titanium [34, 35]. The peaks

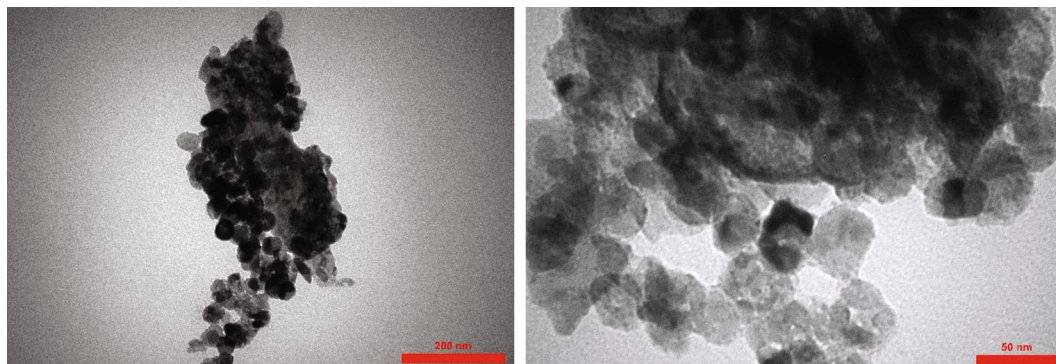


FIGURE 5: The transmitted electron microscope images of xanthan gum/ZnO/TiO₂ nanocomposite at different magnification.

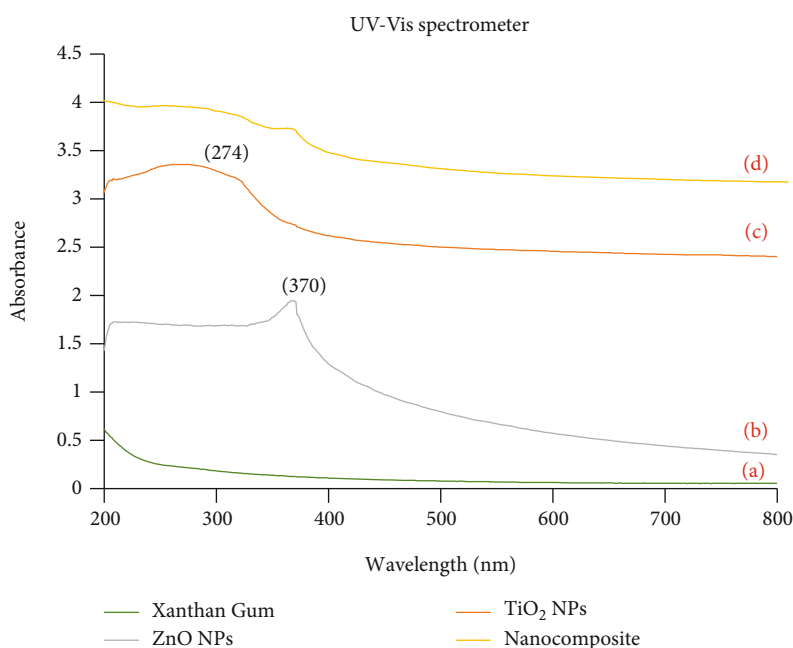


FIGURE 6: UV-visible of xanthan gum (a), ZnO NPs (b), TiO₂ NPs (c), and xanthan gum/ZnO/TiO₂ nanocomposite (d).

observed in the final nanocomposite spectrum (diagram d) showed a combination of peaks in the xanthan gum spectrum and oxide nanoparticles. Therefore, the strong interactions between the components and the formation of the final nanocomposite were confirmed [24].

3.3. XRD Analysis. The X-ray diffraction pattern of Figure 3 is presented to investigate the crystal structure and to identify ZnO NPs (diagram a), TiO₂ nanoparticles (diagram b), and synthesized nanocomposites (diagram c). The X-ray diffraction pattern of ZnO NPs (diagram a) showed the hexagonal crystal structure of the zincite phase for these nanoparticles. Miller indices of (hkl), (100), (002), (101), (102), (110), (103), and (112) were calculated at angles 2θ , 32, 35, 37, 48, 57, 63, and 68 degrees, respectively [36].

The X-ray diffraction pattern of TiO₂NPs (diagram b) showed the anatase phase with a tetragonal crystal structure for this material. Miller indices (hkl), (101), (004), (200), (105), (211), (204), (116), (220), and (215) were calculated

at angles 2θ , 25, 38, 48, 54, 55, 63, 69, 70. and 75 degrees, respectively [37].

X-ray diffraction pattern obtained from synthesized nanocomposite (diagram c) showed the presence of component peaks and their intensity reduction, flattening or removal, and displacement of some peaks relative to the X-ray diffraction pattern of components in the synthesized nanocomposite X-ray diffraction spectrum. In addition, the average crystallite size was calculated for the highest peak of 28 nm.

3.4. SEM and Elemental Mapping Analysis. The appearance and elemental mapping of the xanthan gum/ZnO/TiO₂ nanocomposite were examined by field emission scanning electron microscopy (Figure 4). Figures 4(a) and 4(b) show the placement of metal oxide nanoparticles inside the xanthan gum, resulting in the formation of the final nanocomposite. Elemental mapping was performed by energy-dispersive X-ray spectroscopy (EDS) to evaluate the

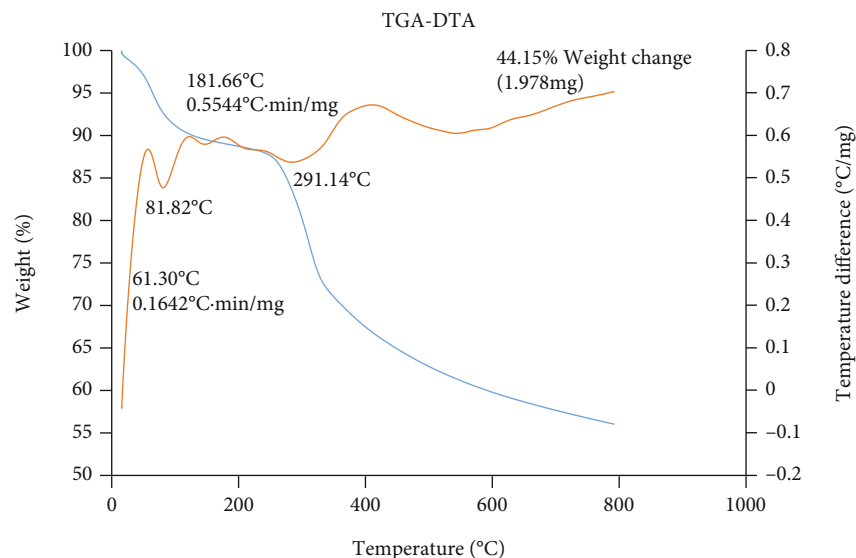


FIGURE 7: Thermogravimetric analysis (TGA-DTA) of xanthan gum/ZnO/TiO₂ nanocomposite.

elemental dispersion in the xanthan gum/ZnO/TiO₂ nanocomposite. Figures 4(c) to 4(f) shows that elements C, O, Zn, and Ti are regularly distributed, confirming the suitable synthesis of the xanthan gum/ZnO/TiO₂ nanocomposite.

3.5. TEM Analysis. The morphology of the xanthan gum/ZnO/TiO₂ nanocomposite was investigated by TEM micrograph preparation of the synthesized nanocomposite. TEM micrograph analysis showed the formation of this nanocomposite (Figure 5). The morphology and distribution of oxide nanoparticles were also examined in more detail by TEM. The results showed that the metal oxide nanoparticles were well in contact with the xanthan gum and the final nanocomposite was prepared by distributing different sizes of particles.

3.6. UV-Vis Analysis. The optical properties of xanthan gum/ZnO/TiO₂ nanocomposite and its components were investigated using ultraviolet-visible spectroscopy in the range of 200 to 800 nm (Figure 6). No specific absorption band was observed in the xanthan gum spectrum (diagram a). In the spectrum of ZnO NPs (diagram b), a sharp and specific peak showed the production of adsorption in the range of 370 nm for this sample. In the spectrum of TiO₂ NPs (diagram c), a wide absorption band with the highest intensity in the range of 274 nm was observed. The absorption spectra of the final synthesized nanocomposite (diagram d) showed the presence of a wide low-intensity absorption peak in the range of 270 nm and a specific low-intensity peak in the range of 371 nm. This confirmed the interaction of the components of the nanocomposite [24].

3.7. Thermal analysis. The thermal properties of xanthan gum/ZnO/TiO₂ nanocomposite composition and its thermal stability were evaluated by TGA and DTA analysis (Figure 7). The behavior of thermogravimetric analysis and differential thermal analysis of the final nanocomposite showed the three main stages of weight loss by 44.15%.

The first stage, consisting of 11% weight loss, occurred in the range of 25–250 °C due to the moisture loss and dehydration of the prepared nanocomposite. The second stage, with a weight loss of 28%, in the temperature range of 250–550 °C, is related to the thermal decomposition of the elements of impurity components and carbon bonds in the nanocomposite. In the last stage of weight loss, with a weight loss of 5.15%, in the temperature range of 550–800 °C, the structural water, which is in the form of bonded hydroxyl groups, begins to decompose and release. In addition, at this stage, impurities with higher thermal stability were decomposed. In the diagram obtained from the differential thermal analysis of the final nanocomposite, exothermic peaks were observed upwards, and endothermic peaks were observed downwards.

4. Conclusions

By analyzing the results of experiments designed by the Taguchi method, the antifungal activity of xanthan gum/ZnO/TiO₂ nanocomposite synthesized by in situ method against *C. albicans* fungal strains was evaluated. The optimal antifungal properties of synthesized nanocomposite were confirmed. Based on the antifungal activity results, it was estimated that the synthesized nanocomposite under the optimal conditions prevents fungal growth up to 95%. Due to the antifungal properties predicted for this nanocomposite, its use as an antimicrobial agent in medicine and dentistry can be effectively useful, and it dramatically reduces pathogenic microbes. Identifying and synthesizing novel and effective antimicrobial compounds can reduce the prevalence of many microbial diseases and prevent increased treatment costs. It is recommended that clinical studies be performed locally and systemically to evaluate the effectiveness of this nanocomposite in the treatment of oral and vaginal candidiasis.

Data Availability

The data used to support the findings of this study are included within the article.

Conflicts of Interest

The authors declare that they have no conflicts of interest.

Acknowledgments

This work was supported by grant number 990429 from the Kermanshah University of Medical Sciences.

References

- [1] A. Zida, S. Bamba, A. Yacouba, R. Ouedraogo-Traore, and R. Guiguemdé, “Substances naturelles actives sur *Candida albicans*, sources de nouveaux médicaments antifongiques : revue de la littérature,” *Journal de Mycologie Médicale*, vol. 27, no. 1, pp. 1–19, 2017.
- [2] M. McCullough, B. Ross, and P. Reade, “*Candida albicans* : a review of its history, taxonomy, epidemiology, virulence attributes, and methods of strain differentiation,” *International Journal of Oral and Maxillofacial Surgery*, vol. 25, no. 2, pp. 136–144, 1996.
- [3] J. A. Parente-Rocha, A. M. Bailão, A. C. Amaral et al., “Anti-fungal resistance, metabolic routes as drug targets, and new antifungal agents: an overview about endemic dimorphic fungi,” *Mediators of Inflammation*, vol. 2017, Article ID 9870679, 2017.
- [4] R. Rezaei, M. Safaei, H. R. Mozaffari et al., “The role of nanomaterials in the treatment of diseases and their effects on the immune system,” *Open Access Macedonian Journal of Medical Sciences*, vol. 7, no. 11, pp. 1884–1890, 2019.
- [5] H. Moradpoor, M. Safaei, F. Rezaei et al., “Optimisation of cobalt oxide nanoparticles synthesis as bactericidal agents,” *Open Access Macedonian Journal of Medical Sciences*, vol. 7, no. 17, pp. 2757–2762, 2019.
- [6] S. El-Sayed, M. Amer, T. Meaz, N. Deghiedy, and H. El-Sher-shaby, “Microstructure optimization of metal oxide nanoparticles and its antimicrobial activity,” *Measurement*, vol. 151, article 107191, 2020.
- [7] M. Taran, M. Safaei, N. Karimi, and A. Almasi, “Benefits and application of nanotechnology in environmental science: an overview,” *Biointerface Research in Applied Chemistry*, vol. 11, no. 1, pp. 7860–7870, 2021.
- [8] A. León-Buitimea, J. A. Garza-Cervantes, D. Y. Gallegos-Alvarado, M. Osorio-Concepción, and J. R. Morones-Ramírez, “Nanomaterial-based antifungal therapies to combat fungal diseases aspergillosis, Coccidioidomycosis, Mucormycosis, and candidiasis,” *Pathogens*, vol. 10, no. 10, p. 1303, 2021.
- [9] S. Keerthana and A. Kumar, “Potential risks and benefits of zinc oxide nanoparticles: a systematic review,” *Critical Reviews in Toxicology*, vol. 50, no. 1, pp. 47–71, 2020.
- [10] H. Moradpoor, M. Safaei, H. R. Mozaffari et al., “An overview of recent progress in dental applications of zinc oxide nanoparticles,” *RSC Advances*, vol. 11, no. 34, pp. 21189–21206, 2021.
- [11] E. Schifano, D. Cavallini, G. De Bellis et al., “Antibacterial effect of zinc oxide-based nanomaterials on environmental biodeteriogens affecting historical buildings,” *Nanomaterials*, vol. 10, no. 2, p. 335, 2020.
- [12] H. M. Ali, H. Babar, T. R. Shah, M. U. Sajid, M. A. Qasim, and S. Javed, “Preparation techniques of TiO₂ nanofluids and challenges: a review,” *Applied Sciences*, vol. 8, no. 4, p. 587, 2018.
- [13] M. Catauro, E. Tranquillo, G. Dal Poggetto, M. Pasquali, A. Dell’Era, and S. Vecchio Cipriotti, “Influence of the heat treatment on the particles size and on the crystalline phase of TiO₂ synthesized by the sol-gel method,” *Materials*, vol. 11, no. 12, p. 2364, 2018.
- [14] C. L. de Dicastillo, C. Patiño, M. J. Galotto et al., “Novel hollow titanium dioxide nanospheres with antimicrobial activity against resistant bacteria,” *Beilstein Journal of Nanotechnology*, vol. 10, no. 1, pp. 1716–1725, 2019.
- [15] S. Mathew, P. Ganguly, V. Kumaravel et al., “Effect of chalcogens (S, Se, and Te) on the anatase phase stability and photocatalytic antimicrobial activity of TiO₂,” *Materials Today: Proceedings*, vol. 33, pp. 2458–2464, 2020.
- [16] G. De Falco, A. Porta, P. Del Gaudio, M. Commodo, P. Minutolo, and A. D’Anna, “Antimicrobial activity of TiO₂ coatings prepared by direct thermophoretic deposition of flame-synthesized nanoparticles,” *MRS Advances*, vol. 2, no. 28, pp. 1493–1498, 2017.
- [17] C. Liao, Y. Li, and S. C. Tjong, “Visible-light active titanium dioxide nanomaterials with bactericidal properties,” *Nanomaterials*, vol. 10, no. 1, p. 124, 2020.
- [18] D. R. A. Muhammad, A. S. Doost, V. Gupta et al., “Stability and functionality of xanthan gum–shellac nanoparticles for the encapsulation of cinnamon bark extract,” *Food Hydrocolloids*, vol. 100, article 105377, 2020.
- [19] M. K. Schnizlein, K. C. Vendrov, S. J. Edwards, E. C. Martens, and V. B. Young, “Dietary xanthan gum alters antibiotic efficacy against the murine gut microbiota and attenuates *Clostridioides difficile* colonization,” *Mosphere*, vol. 5, no. 1, pp. 708–719, 2020.
- [20] M. H. A. Elella, M. Sabaa, D. H. Hanna, M. M. Abdel-Aziz, and R. R. Mohamed, “Antimicrobial pH-sensitive protein carrier based on modified xanthan gum,” *Journal of Drug Delivery Science and Technology*, vol. 57, article 101673, 2020.
- [21] Z. Wang, Q. Yang, X. Wang et al., “Antibacterial activity of xanthan-oligosaccharide against *Staphylococcus aureus* via targeting biofilm and cell membrane,” *International Journal of Biological Macromolecules*, vol. 153, pp. 539–544, 2020.
- [22] A. Karami, “Synthesis of TiO₂ nano powder by the sol-gel method and its use as a photocatalyst,” *Journal of the Iranian Chemical Society*, vol. 7, no. S2, pp. S154–S160, 2010.
- [23] R. E. Adam, G. Pozina, M. Willander, and O. Nur, “Synthesis of ZnO nanoparticles by co-precipitation method for solar driven photodegradation of Congo red dye at different pH,” *Photonics and Nanostructures - Fundamentals and Applications*, vol. 32, pp. 11–18, 2018.
- [24] M. Safaei, M. Taran, L. Jamshidy et al., “Optimum synthesis of polyhydroxybutyrate-Co₃O₄ bionanocomposite with the highest antibacterial activity against multidrug resistant bacteria,” *International Journal of Biological Macromolecules*, vol. 158, pp. 477–485, 2020.
- [25] B. Das, M. I. Khan, R. Jayabalan et al., “Understanding the antifungal mechanism of Ag@ZnO core-shell nanocomposites against *Candida krusei*,” *Scientific Reports*, vol. 6, no. 1, p. 36403, 2016.
- [26] S. Wang, J. Wu, H. Yang, X. Liu, Q. Huang, and Z. Lu, “Antibacterial activity and mechanism of Ag/ZnO nanocomposite

- against anaerobic oral pathogen *Streptococcus mutans*,” *Journal of Materials Science: Materials in Medicine*, vol. 28, no. 1, p. 23, 2017.
- [27] S. Gharpure, A. Akash, and B. Ankamwar, “A review on antimicrobial properties of metal nanoparticles,” *Journal of Nanoscience and Nanotechnology*, vol. 20, no. 6, pp. 3303–3339, 2020.
- [28] A. I. Raafat, N. M. El-Sawy, N. A. Badawy, E. A. Mousa, and A. M. Mohamed, “Radiation fabrication of xanthan-based wound dressing hydrogels embedded ZnO nanoparticles: in vitro evaluation,” *International Journal of Biological Macromolecules*, vol. 118, Part B, pp. 1892–1902, 2018.
- [29] N. N. Ilkhechi, M. Mozammel, and A. Y. Khosroushahi, “Anti-fungal effects of ZnO, TiO₂ and ZnO- TiO₂ nanostructures on *Aspergillus flavus*,” *Pesticide Biochemistry and Physiology*, vol. 176, article 104869, 2021.
- [30] M. Safaei, M. Taran, and M. M. Imani, “Preparation, structural characterization, thermal properties and antifungal activity of alginate-CuO bionanocomposite,” *Materials Science and Engineering C*, vol. 101, pp. 323–329, 2019.
- [31] T. R. Lakshmeesha, M. Murali, M. A. Ansari et al., “Biofabrication of zinc oxide nanoparticles from *Melia azedarach* and its potential in controlling soybean seed-borne phytopathogenic fungi,” *Saudi Journal of Biological Sciences*, vol. 27, no. 8, pp. 1923–1930, 2020.
- [32] M. H. A. Elella, E. S. Goda, H. M. Abdallah, A. E. Shalan, H. Gamal, and K. R. Yoon, “Innovative bactericidal adsorbents containing modified xanthan gum/montmorillonite nanocomposites for wastewater treatment,” *International Journal of Biological Macromolecules*, vol. 167, pp. 1113–1125, 2021.
- [33] P. G. Devi and A. S. Velu, “Synthesis, structural and optical properties of pure ZnO and co doped ZnO nanoparticles prepared by the co-precipitation method,” *Journal of Theoretical and Applied Physics*, vol. 10, no. 3, pp. 233–240, 2016.
- [34] A. Fahami, R. Ebrahimi-Kahrizsangi, and B. Nasiri-Tabrizi, “Mechanochemical synthesis of hydroxyapatite/titanium nanocomposite,” *Solid State Sciences*, vol. 13, no. 1, pp. 135–141, 2011.
- [35] R. B. KC, C. K. Kim, M. S. Khil, H. Y. Kim, and I. S. Kim, “Synthesis of hydroxyapatite crystals using titanium oxide electrospun nanofibers,” *Materials Science and Engineering: C*, vol. 28, no. 1, pp. 70–74, 2008.
- [36] S. Getie, A. Belay, A. Chandra Reddy, and Z. Belay, “Synthesis and characterizations of zinc oxide nanoparticles for antibacterial applications,” *Journal of Nanomedicine and Nanotechnology*, vol. s8, p. 004, 2017.
- [37] X. Wei, G. Zhu, J. Fang, and J. Chen, “Synthesis, characterization, and photocatalysis of well-dispersible phase-pure anatase TiO₂ nanoparticles,” *International Journal of Photoenergy*, vol. 2013, Article ID 726872, 2013.

Research Article

Antibacterial, Cytotoxic, and Cellular Mechanisms of Green Synthesized Silver Nanoparticles against Some Cariogenic Bacteria (*Streptococcus mutans* and *Actinomyces viscosus*)

Hanaa Ghabban ¹, Sultan F. Alnomasy ², Hamdan Almohammed ³,
Ohoud M. Al Idriss ⁴, Sameh Rabea ⁵, and Yasir Eltahir ⁶

¹Department of Biology, Faculty of Science, University of Tabuk, Tabuk, Saudi Arabia

²Department of Medical Laboratories Sciences, College of Applied Medical Sciences in Al-Quwayyah, Shaqra University, 19257, Saudi Arabia

³Department of Basic Medical Sciences, College of Medicine, AlMaarefa University, Riyadh, Saudi Arabia

⁴Department of Clinical Laboratory, College of Applied Medical Sciences, King Saud University, Riyadh, Saudi Arabia

⁵Department of Pharmaceutical Sciences, College of Pharmacy, AlMaarefa University, Riyadh, Saudi Arabia

⁶Department of Respiratory Therapy, College of Applied Sciences, AlMaarefa University, Riyadh, Saudi Arabia

Correspondence should be addressed to Hanaa Ghabban; h_ghabban@ut.edu.sa

Received 1 December 2021; Revised 6 January 2022; Accepted 19 January 2022; Published 9 February 2022

Academic Editor: Seyed alireza Hashemi

Copyright © 2022 Hanaa Ghabban et al. This is an open access article distributed under the Creative Commons Attribution License, which permits unrestricted use, distribution, and reproduction in any medium, provided the original work is properly cited.

Background. The present study focused on the green synthesis of silver nanoparticles (AgNPs) using the *Astragalus spinosus* Forssk. aqueous extract. In addition, we evaluated the antibacterial activity of AgNPs as well as some cellular mechanisms against *Actinomyces viscosus* and *Streptococcus mutans* as the most causative agents of tooth decay. **Methods.** In this study, AgNPs were green synthesized by the precipitation method based on the reduction of silver ions (AgNO₃) by *A. spinosus* extract. Antibacterial effects of the green synthesized AgNPs were performed by measuring the minimum inhibitory concentration (MIC) and minimum bactericidal concentrations (MBC) through micro broth dilution method. In addition, we evaluated the reactive oxygen species (ROS) production, nucleic acid leakage, and protein leakage as the main antibacterial mechanisms of the green synthesized AgNPs against *A. viscosus* and *S. mutans*. The cytotoxicity effects of AgNPs against human normal (NOF18 cells) and oral cancer (SCC4 cells) cell lines were also evaluated using MTT assay. **Results.** The green synthesized AgNPs have a spherical shape and are relatively uniform in size in the range of 30-40 nm. The MIC values for *S. mutans* and *A. viscosus* of the green synthesized AgNPs were 10.6 and 13.3 µg/ml, respectively, whereas the MBC values for *S. mutans* and *A. viscosus* of the green synthesized AgNPs were 21.3 and 26.6 µg/ml. The findings exhibited that ROS production, nucleic acid leakage, and protein leakage were increased after treatment of *A. viscosus* and *S. mutans* by the green synthesized AgNPs. The results demonstrated that the 50% inhibitory concentration (IC₅₀) values of AgNPs on NOF18 and SCC4 cells were 93.3 µg/ml and 41.2 µg/ml, respectively. **Conclusion.** Overall, the results of this study showed that *A. spinosus* extract has a good ability to produce silver nanoparticles. The AgNPs produced have significant antibacterial effects against some tooth decay bacteria. Our results also revealed that the green synthesized AgNPs are more cytotoxic against cancerous cell line than normal cell line. Further *in vivo* studies are required to investigate the side effects and to evaluate the effectiveness of these bacteria.

1. Introduction

Dental caries as a permanent damage in the enamel or hard surface of the teeth is a chronic microbial disease affecting

humans worldwide [1]. Based on the World Health Organization (WHO) reports, the frequency of dental caries varies ranging from 60 to 80% in children and nearly 100% in adult people [2]. The oral cavity is an exceptional ecological site

TABLE 1: The minimum inhibitory concentration (MIC) and the minimum bactericidal concentrations (MBC) of the green synthesized AgNPs by *A. spinosus* extract on *S. mutans* and *A. viscosus*.

Drug	<i>A. viscosus</i>		<i>S. mutans</i>	
	MIC ($\mu\text{g}/\text{ml}$)	MBC ($\mu\text{g}/\text{ml}$)	MIC ($\mu\text{g}/\text{ml}$)	MBC ($\mu\text{g}/\text{ml}$)
AgNPs	13.33 ± 4.6	26.66 ± 4.6	10.6 ± 4.6	21.33 ± 1.15
Chlorhexidine	10.6 ± 4.6	21.33 ± 1.15	8.0 ± 0.0	16.0 ± 0.0

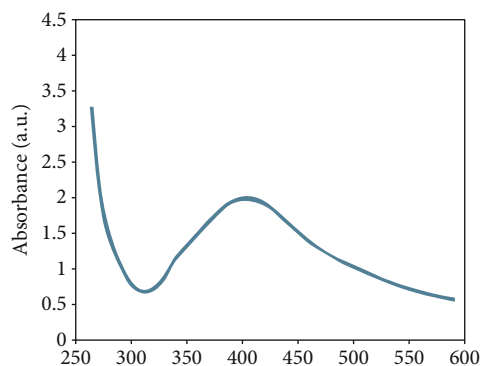


FIGURE 1: Ultraviolet absorption by silver nanoparticle green synthesized from the *A. spinosus* extract.

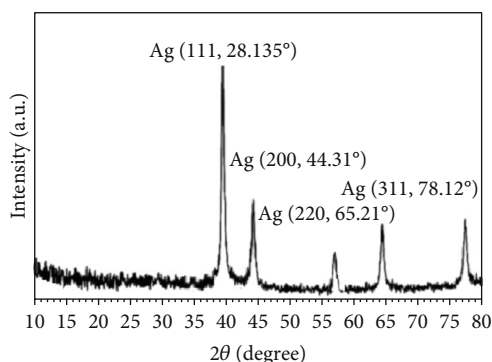


FIGURE 2: X-ray diffraction (XRD) analysis of the green synthesized AgNPs.

for microorganisms, where most of these microorganisms multiply on tooth surfaces and cause dental plaque (oral biofilm) [3]. The cariogenic bacteria are among the oral microbiota that ferment carbohydrates and subsequently produce acids and demineralize the tooth surfaces. Such bacteria, including *Streptococcus* spp., *Actinomyces* spp., and *Nocardia* spp., are well-known as the main cariogenic causes involved in the progress of tooth caries [3, 4]. Because of the available systemic antibiotics are not effective for treating oral bacteria or not specific to treat oral diseases, several antimicrobial agents such as chlorhexidine, fluoride, and quaternary ammonium salts have been used to target oral bacteria that cause oral diseases such as tooth decay [5].

Today, metal nanoparticles are used as attractive candidates to deliver many small drug molecules or large biomol-

ecules [6]. Metal nanoparticles are widely used as important products in nanomedicine due to their unique physical properties [7]. Recently, studies have demonstrated that the chemical and physical techniques used to synthesize nanoparticles are often very expensive, and the presence of toxic and sometimes carcinogenic residues that produced these techniques usually results in harming effects of the nanoparticles [8]. Therefore, the development of reliable, nontoxic, and cost-effective methods for the synthesis of nanoparticles using plants (green synthesis) and microorganisms is highly valuable. Today, the use of plants as a renewable and inexpensive source for the synthesis of green nanoparticles has received much attention [9].

The existence of the secondary metabolites (e.g., polyphenols, alkaloids, terpenoids, quinones, and tannins) in plants encourages ion bioremediation and synthesis of some metal nanoparticles [10]. Among metal nanoparticles, silver nanoparticles (AgNPs) have emerged as a powerful product in the field of nanotechnology [11]. These nanoparticles have received special attention over the past few years due to their proper conductivity, chemical stability, catalytic activity, and antimicrobial properties [12]. *Astragalus* plants belonging to the Fabaceae family (with more than 3000 species) are one of the most important plant species around the world [13]. In traditional medicine, plants of the genus *Astragalus* were used for treating diseases and illness conditions such as bronchitis, cough, stomach ulcer, hypertension, gynecological disorders, and diabetes [14]. In modern medicine, previous studies also demonstrated that plants of *Astragalus* genus have some pharmacological properties such as anti-inflammatory, antidiabetic, anticancer, antioxidant, analgesic, and antioxidant [15].

The present study is aimed at green synthesis and characterization of the AgNPs using the *Astragalus spinosus* Forssk. aqueous extract. The study is also targeting the evaluation of the antibacterial activity of the AgNPs as well as some cellular mechanisms against *Actinomyces viscosus* and *Streptococcus mutans* as the most common agents in tooth decay.

2. Materials and Methods

2.1. Plant Materials and Extraction. Aerial parts of *A. spinosus* were obtained from country districts of Tabuk, Saudi Arabia, in April 2020. The collected herbs were then recognized by a botanist, and a sample of voucher of the herb was archived at the herbarium of College of Applied Medical Sciences, Al-Qwayyah, Shaqra University, Saudi Arabia, for further experiments. Air dried fruits of *A. spinosus* (200 g) were extracted through percolation process with water consecutively for 3 days at 21°C. In the next step, the extracts were filtered by using filter paper (Sigma, Germany) and lastly evaporated in vacuum at 55°C by means of a rotary evaporator and preserved at -20°C until examining.

2.2. Green Synthesis of AgNPs. In this study, AgNPs were green synthesized by the precipitation method based on the reduction of silver ions (AgNO_3) through *A. spinosus* extract according to the method described by Sulaiman et al. [16]. To do this, 10 ml of the extract was added to

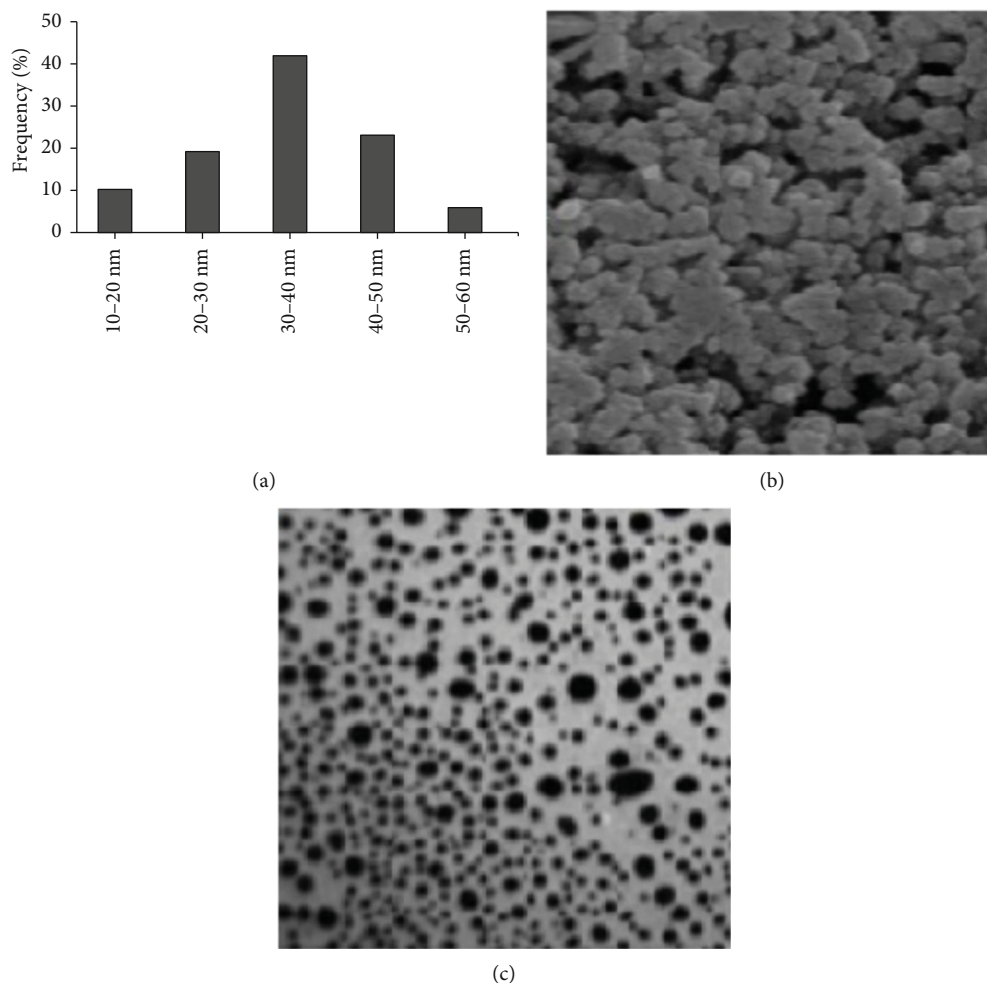


FIGURE 3: (a) The size distribution of the green synthesized AgNPs by *Astragalus spinosus* extract; (b) scanning electron microscope (SEM) and (c) transmission electron microscopy (TEM) of the green synthesized AgNPs displayed a spherical shape and are relatively uniform in size in the range of 30-40 nm.

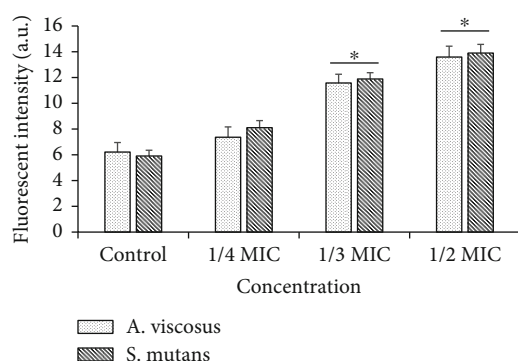


FIGURE 4: The reactive oxygen species (ROS) production of AgNPs on *S. mutans* and *A. viscosus*. Data are presented as Mean \pm SD. * $p < 0.001$.

90 ml of AgNO_3 (1 Mm, Merck, Germany) and kept at room temperature and in the dark overnight to reduce silver ions and to reduce ions. The change in color of the extract from pale yellow to dark brown to black indicates the production

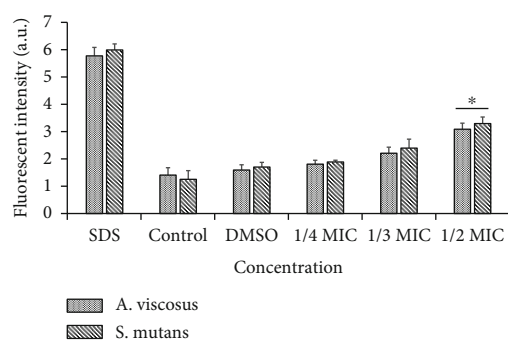
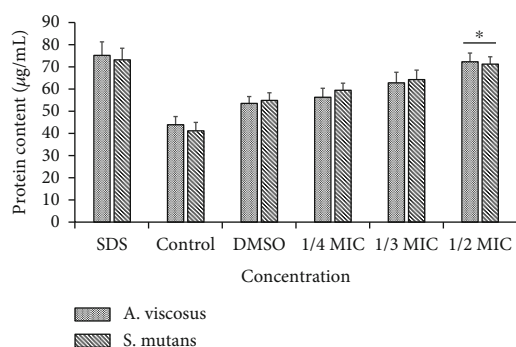
of AgNO_3 . In order to observe the color changes on the absorbance of the solution, a spectrophotometer in the range of 300-700 nm was investigated. The solution containing the nanoparticles was centrifuged at 12000 rpm for 15 minutes, and then, the supernatant was discarded.

2.3. UV-vis Spectroscopy Analysis. Surface plasmon resonance (SPR) of synthesized AgNPs was determined by using UV-vis spectrophotometer to approve the transformation of the Ag ions to AgNPs. Accordingly, 0.3 ml of the NPS solution was diluted with 3 ml of normal saline and was examined by UV-vis spectrum analysis employing a spectrophotometer device (Shimadzu UV2550, Japan) in the range of 300-700 nm.

2.4. X-Ray Diffraction (XRD) Analysis. XRD analysis was used to investigate the presence of nanoparticles by *A. spinosus* extract. In fact, this method examines the stepwise formation of biodegradable nanoparticles. The crystal structure of the synthesized nanoparticles was investigated by considering the Ka ray source of a copper lamp with a

TABLE 2: Some recent studies and their research findings on the green synthesis of silver nanoparticles (AgNPs) using various plants.

Authors	Years	Plant name	Results	Ref.
Emrani et al.	2018	<i>Glycyrrhiza glabra</i> and <i>Mentha piperata</i>	MIC values for AgNPs synthesized with <i>G. glabra</i> extract against <i>Streptococcus mutans</i> , <i>Actinomyces viscosus</i> , and <i>Lactobacillus rhamnosus</i> were 1.6, 6.25, and 50 mg/ml, and MIC for AgNPs synthesized with <i>Mentha piperata</i> extract against these bacteria were determined to be 12.5, 12.5, and 200 mg/ml, respectively	[29]
Majeed et al.	2016	<i>Salix alba</i>	These synthesized silver nanoparticles showed a good antibacterial activity against the bacteria isolates (<i>Lactobacillus</i> sp., <i>Streptococcus</i> sp., and <i>Staphylococcus</i> sp.)	[30]
Suwan et al.	2018	<i>Oryza sativa</i> L.	Antimicrobial test showed that the AgNPs obtained from green synthesis mediated by rice extracts have great antimicrobial activity against <i>Streptococcus mutans</i>	[23]
Hernández-Gómora et al.	2017	<i>Heterotheca inuloides</i>	AgNPs exhibited antibacterial activity against <i>Streptococcus mutans</i> , <i>Lactobacillus casei</i> , <i>Staphylococcus aureus</i> , and <i>Escherichia coli</i>	[31]
Tolouietabar et al.	2017	<i>Scrophularia striata</i>	AgNPs at the concentration of 5 mM showed significant antibacterial activity against <i>Escherichia coli</i> , <i>Salmonella typhi</i> , <i>Klebsiella pneumoniae</i> , <i>Staphylococcus aureus</i> , and <i>Bacillus cereus</i>	[32]

FIGURE 5: Effects of the green synthesized AgNPs on nucleic acid leakage from *S. mutans* and *A. viscosus* cells at 1/2 MIC, MIC, and 2 MIC. Data are presented as Mean \pm SD. * $p < 0.001$.FIGURE 6: Effects of the green synthesized AgNPs on protein leakage from *S. mutans* and *A. viscosus* cells at 1/2 MIC, MIC, and 2 MIC. Data are presented as Mean \pm SD. * $p < 0.001$.

wavelength of X beams in $\lambda = 1.54 \text{ \AA}$ by a XRD device model 2000 APD (Italy).

2.5. Dynamic Light Scattering (DLS) and Electron Microscope. The specifications of synthesized AgNPs such as morphology (the size and shape) were studied by scanning electron microscope (SEM) (Mira3, made in Czech) with 15 kV, magnification of 10x, and resolution of 1 nm as well as transmission electron microscopy (TEM, Jeol JEM-

1220, JEOL, Japan). In this study, the particle size was determined through DLS using the Zetasizer (UK, Malvern) device.

2.6. Antibacterial Effect of NPs

2.6.1. Bacteria. Each of the bacterial species of *S. mutans* (ATCC 35668) and *A. viscosus* (PTCC 1202) was cultured in Tryptic Soy Broth (TSB) Agar, Brain Heart Infusion (BHI, Difco, USA), and Mitis Salivarius Agar (MSA) at 37°C in an atmosphere containing 5% CO₂. Finally, growing bacteria were confirmed by means of Gram staining, catalase test, optochin, and bacitracin tests.

2.6.2. Preparation of Standard McFarland 0.5 Solution. To prepare the standard McFarland 0.5 solution, 0.5 ml of BaCl₂ (0.048 mol/l) (2H₂O w/v BaCl₂ 1/175%) was added to 99.5 ml of sulfuric acid (0.18 mol/l) (v/v 1%). The suspension was stirred constantly, and the standard optical density was evaluated by absorbance measurement by means of a spectrophotometer at an optical length of 1 cm. The absorbance of 625 nm should be between 0.8 and 0.13 [17].

2.6.3. Preparation of 0.5 McFarland Solution of Studied Bacteria. Some colonies of bacteria were dissolved in 1 cc of physiological serum. Turbidity of bacterial solution was compared with the standard 0.5 McFarland solution [17].

2.6.4. Micro Broth Dilution. The minimum inhibitory concentration (MIC) of green synthesized AgNPs against *S. mutans* and *A. viscosus* was evaluated by micro broth dilution method based on the Clinical and Laboratory Standards Institute (CLSI) orders [18]. Initially, a stock of synthesized AgNPs is prepared with normal saline solvent and sterile Müller-Hinton broth culture medium. Then, 50 microliters of sterile Müller Hinton broth culture medium was added to the third to twelfth rows. From the stock made, 100 microliters is added to the first and second rows, and the dilution operation is performed from the second to the tenth rows. In this way, from the second row, 50 microliters to the third row and from the third row 50 microliters to the fourth row and up to the tenth row will be diluted in the same way.

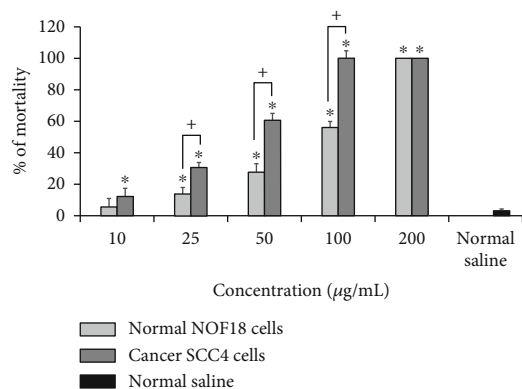


FIGURE 7: The cytotoxicity effects of the green synthesized AgNPs against human normal (NOF18 cells) and oral cancer (SCC4 cells) cell lines, which were evaluated using the colorimetric MTT (3-(4,5-dimethylthiazol-2-yl)-2,5-diphenyltetrazolium bromide) assay. Mean \pm SD ($n = 3$). * $p < 0.001$ difference was statistically significant compared with the control group (normal saline). + $p < 0.001$ difference was statistically significant.

Finally, after 24 hours of culture, the desired microorganism is added in the amount of 50 microliters equivalent to half McFarland turbidity (1.5×10^8 cfu/ml) to two to ten rows. The plates are placed in a shaker incubator for 24 hours at 37°C, and then, salts of 2, 3, and 5-triphenyltetrazolium chloride are used as a visual indicator for bacterial growth. Colorless wells are reported as MICs. The lowest concentration of the AgNPs in which no bacteria survived was considered to indicate the minimum bactericidal concentrations (MBC) of AgNPs. Normal saline is used for negative control, and chlorhexidine is used for positive control.

2.6.5. Analysis of the Reactive Oxygen Species (ROS) Generation. In the present investigation, we used 2', 7'-dichlorofluorescein diacetate (DCFH-DA, Sigma-Aldrich, Germany) to determine the level of bacterial ROS prompted by synthesized AgNPs. In summary, *S. mutans* and *A. viscosus* cells were separately incubated with 10 µM of DCFH-DA at 37°C for 30 min. Next, bacteria were separately treated with and without the green synthesized AgNPs at the concentrations of 1/2 MIC, 1/3 MIC, and 1/4 MIC for 3 h. Finally, the fluorescence intensity was measured at excitation/emission wavelength of 488/525 nm [19].

2.7. Effects of the Green Synthesized AgNPs on Nucleic Acid Leakage. In this study, we evaluated the effect of green synthesized AgNPs on the integrity of bacterial membranes, based on the methods described elsewhere [20]. Briefly, the bacteria suspension was treated with the green synthesized AgNPs at the concentrations of 1/4 MIC, 1/3 MIC, and 1/2 MIC and was incubated at 37°C for 30 min. In the next step, 1 ml of the bacteria was centrifuged for 1 minute at 10,000 rpm; the obtained residual sediment was washed with 1 ml normal saline, and then, the 3 µl of propidium iodide was added to the combination and kept for 10 minutes in the dark. Fluorescence was measured at excitation and emission wavelengths of 544 nm and 612 nm, respectively, using

a *f*max microplate spectrofluorometer (Molecular Devices, Sunnyvale, USA). The negative and positive controls were contained dimethyl sulfoxide (DMSO) and sodium dodecyl sulphate (SDS, 0.1%).

2.8. Effects of the Green Synthesized AgNPs on Protein Leakage. Here, we determined the effects of the green synthesized AgNPs on protein leakage based on the method explained by Du et al. [21]. In brief, the bacteria suspension was treated with the green synthesized AgNPs at the concentrations of 1/4 MIC, 1/3 MIC, and 1/2 MIC and was incubated at 37°C with shaking for 120 min. In the next step, after centrifuging the bacteria suspensions at 4000 rpm for 240 s, 0.05 ml of the suspensions supernatant was mixed with 0.95 ml of Bradford reagent. Finally, the protein content was assessed according to the Bradford's method [22]. The negative and positive controls were contained dimethyl sulfoxide (DMSO) and sodium dodecyl sulphate (SDS, 0.1%). The absorbance was measured at 590 nm using a microplate reader spectrophotometer (BioTek Winooski, VT, USA).

2.9. Cytotoxicity Effects. The cytotoxic effects of the green synthesized AgNPs against human oral squamous cell carcinoma cells (SCC4, American Type Culture Collection/ATCC CRL-1624) and human normal oral fibroblasts (NOF18) were evaluated using the colorimetric MTT assay (3-(4,5-dimethylthiazol-2-yl)-2,5-diphenyltetrazolium bromide) according to the method described elsewhere [23]. SCC4 and NOF cell lines were cultured in Dulbecco's Modified Eagle Medium (DMEM) (UFC-Biotech, SA) supplemented with 15% (*v/v*) fetal bovine serum (FBS) (Thermo Fisher, USA), penicillin (100 IU/ml), and streptomycin (100 µg/ml) (UFC-Biotech, SA). Then, SCC4 and NOF18 cells (5×10^4 /ml) were treated with the green synthesized AgNPs (10–200 µg/ml) for 48 h in microplates at 37°C with 5% CO₂ [24, 25].

2.10. Statistical Analysis. All statistical tests were carried out using the SPSS software version 25.0 (SPSS, Inc.). To compare the results among tested groups, we applied the unpaired sample *t*-test and one-way analysis of variance (ANOVA) and the Dunnett's test. $p < 0.05$ was measured statistically significant.

3. Results and Discussion

Nanoparticles have a major impact on all aspects of human life due to their special properties such as size, shape, and morphology, and among them, metal nanoparticles such as silver, gold, platinum, and palladium have many applications in various scientific fields such as medical engineering and health [26]. The synthesis of silver nanoparticles has long been widespread due to some of their biological properties such as anticancer, antibacterial, antioxidant, and other effects [12]. Today, the use of plants as sustainable and available sources in the production of biocompatible nanoparticles has been considered by many researchers in recent years, and the advantages of this method include biocompatibility, cheapness, nontoxicity, and production of high purity nanoparticles [27]. It has already been proven that

compounds, secondary metabolites, and biomolecules such as carbohydrates, lipids, phenols, flavonoids, tannins, acids, resins, and terpenes in plants play an important role in reducing nanoparticle ions [10]. In recent decades, there has been a growing attention of research on the efficiency of green synthesized nanoparticles on numerous diseases, including microbial infections [6, 7], although various laboratory and experimental investigations have reported the promising antiparasitic effects of silver nanoparticle green synthesized using various natural resource against a wide range of Gram-negative and Gram-positive bacteria; however, their efficacy as well as their toxicity is still debatable and questionable (Table 1) [23, 28–32]. The present study is aimed at green synthesis and characterization of the AgNPs using the *A. spinosus* methanolic extract. In addition, we evaluated the antibacterial activity of the AgNPs as well as some cellular mechanisms against *A. viscosus* and *S. mutans* as the most common agents in tooth decay.

The obtained results demonstrated that complete reduction of Ag^+ ions to AgNPs was performed by changing the color of the culture medium and spectroscopy. The change in color of the sample to dark brown is a clear sign of the synthesis of silver nanoparticles. The presence of a peak at 413 nm by UV-vis spectroscopy confirmed the synthesis of AgNPs (Figure 1). Since the peak formed at a wavelength of 400 to 450 nm indicates the formation of silver nanoparticles and is related to the surface plasmon resonance of silver nanoparticles, which is attributed to the induction of free electrons in nanoparticles, Figure 2 shows the XRD analysis of AgNP green synthesized from the *A. spinosus* extract. The XRD pattern showed that peaks 111, 200, 220, and 311 at 28.135° , 44.31° , 65.21° , and 78.12° corresponded to nanocrystals and silver cubic structures. Nonappearance of other peaks confirmed the purity of AgNPs used in the analysis. The size distribution of the of the green synthesized AgNPs was in the range among 5–60 nm, while the most common particles of the green synthesized AgNPs had the size of 30–40 nm (Figure 3(a)). As shown in Figures 3(b) and 3(c), by TEM and SEM, the green synthesized AgNPs have a spherical shape and are relatively uniform in size in the range of 30–40 nm.

In order to measure the electrophoretic mobility and charge of each nanoparticle sample, we performed the zeta potential experiment, whereas the high zeta potential value exhibited a high electric charge on the surface of the NPs that indicates promising repellent forces among the particles, which inhibits aggregation and result in stabilizing the NPs in the medium. Based on the obtained results, the optimal conditions (pH = 7.2), the value for the zeta potential was -14.6 and width (mV) with 100% intensity and indicated that the synthesized AgNPs are stable because of the electrostatic repulsion without adding a different physical or chemical capping agent (Figure 4).

Considering the antibacterial effects of green synthesized AgNPs, as shown in Table 1, the MIC values of green synthesized AgNPs for *S. mutans* and *A. viscosus* were 10.6 and 13.3 $\mu\text{g}/\text{ml}$, respectively, whereas the MBC values for *S. mutans* and *A. viscosus* of the green synthesized AgNPs were 21.3 and 26.6 $\mu\text{g}/\text{ml}$, respectively. Previous studies demon-

strated the antibacterial effects of AgNPs synthesized from a number of plants (e.g., *Theobroma cacao*, *Pteridium aquilinum*, *Aloe vera*, *Mangifera indica*, *Azadirachta indica*, *Solanum indicum*, and *Ziziphus xylopyrus*) against both Gram-positive and Gram-negative bacteria such as *Staphylococcus aureus*, *Staphylococcus epidermidis*, *Basillus* spp., *Escherichia coli*, *Salmonella typhi*, *Shigella flexneri*, and *Klebsiella pneumoniae* [33] (Table 2).

By DCFH-DA assay, we assessed that whether antibacterial effects of the green synthesized AgNPs may be related to ROS. As shown in Figure 4, although fluorescence intensity was increased in a dose-dependent manner, however, a significant increase ($p < 0.05$) was observed at the concentration of 1/3 MIC and 1/2 MIC. These findings indicated that the green synthesized AgNPs mediated ROS production compared with that of the control group. It has been proven that ROS prompted by nanoparticles can cause the disruption in biomolecules and organelle structures and result in protein oxidative carbonylation, peroxidation of lipids, DNA/RNA rupture, and membrane structure damage, which further result in cell death [34].

As exhibits in Figure 5, the membrane disruption of bacteria was observed by an increased uptake of propidium iodide by *S. mutans* and *A. viscosus* cells treated with the green synthesized AgNPs in a dose-dependent manner. A significant nucleic acid leakage ($p < 0.05$) from bacteria cells was observed after treatment with 1/2 MIC of AgNP when compared to the control, whereas at concentrations of 1/3 MIC and 1/4 MIC, the green synthesized AgNPs were not able to cause significant nucleic acid leakage from bacteria cells in comparison with the control. Figure 6 shows the protein content after exposure of *S. mutans* and *A. viscosus* with the green synthesized AgNPs at the concentrations of 1/2 MIC, 1/3 MIC, and 1/4 MIC. The results exhibited that the green synthesized AgNPs displayed significant ($p < 0.05$) protein leakage at 1/2 MIC. However, at concentrations of 1/3 MIC and 1/4 MIC, there was no significant protein leakage in comparison with the control untreated cells. In line with our results, Rajesh et al. have demonstrated that silver nanoparticles are able to increase the protein leakage through the membrane of *Klebsiella pneumoniae* [35]. In addition, Abbaszadegan et al. have revealed that AgNPs displayed its antibacterial effects against some Gram-positive and Gram-negative bacteria through the protein leakage from the cell [36]. Therefore, the findings of the present study exhibited that ROS production, nucleic acid leakage, and protein leakage are the main antibacterial mechanisms of the green synthesized AgNPs against *A. viscosus* and *S. mutans*.

Here, the cytotoxicity effects of the green synthesized AgNPs against on normal (NOF18 cells) and cancer (SCC4 cells) cell lines were evaluated using MTT assay via measuring their IC_{50} values. Figure 7 shows the cytotoxicity effects of the green synthesized AgNPs against on NOF18 and SCC4 cell lines 48 h. The results demonstrated that the IC_{50} of AgNP value for NOF18 and SCC4 cells were 93.3 $\mu\text{g}/\text{ml}$ and 41.2 $\mu\text{g}/\text{ml}$, respectively. Previously, Khorrami et al. have evaluated the cytotoxicity effects of AgNPs synthesized from *Juglans regia* extract against L-929

fibroblast normal cells and MCF-7 cells [37]; in line with our results, they have reported that the green synthesized AgNPs are cytotoxic against cancerous cell line while being nontoxic for normal cell line.

4. Conclusion

Overall, the results of this study showed that *A. spinosus* extract has a good ability to produce silver nanoparticles. The AgNPs produced have significant antibacterial effects against some tooth decay bacteria. Our results also revealed that the green synthesized AgNPs are more cytotoxic against cancerous cell line than normal cell line. Further *in vivo* studies are required to investigate the side effects and to evaluate the effectiveness of these bacteria. Therefore, this promising silver nanoparticle green synthesized using the *A. spinosus* Forssk. aqueous extract can be used in antimicrobial mouthwashes, prophylactic antibiotics, dental implants, and toothbrushing techniques after final approvals.

Data Availability

All data generated or analyzed during this study are included in this published article.

Consent

No consent was necessary.

Conflicts of Interest

All authors declare that they have no competing interests.

Acknowledgments

The authors deeply acknowledge the Researchers Supporting Program (TUMA-Project-2021-33), Almaarefa University, Riyadh, Saudi Arabia, for supporting steps of this work.

References

- [1] R. H. Selwitz, A. I. Ismail, and N. B. Pitts, "Dental caries," *The Lancet*, vol. 369, no. 9555, pp. 51–59, 2007.
- [2] P. E. Petersen, D. Bourgeois, H. Ogawa, S. Estupinan-Day, and C. Ndiaye, "The global burden of oral diseases and risks to oral health," *Bulletin of the World Health Organization*, vol. 83, pp. 661–669, 2005.
- [3] D. Beighton, "Can the ecology of the dental biofilm be beneficially altered?," *Advances in Dental Research*, vol. 21, no. 1, pp. 69–73, 2009.
- [4] K. Yadav and S. Prakash, "Dental caries: a review," *Asian Journal of Biomedical and Pharmaceutical Sciences*, vol. 6, no. 53, p. 1, 2016.
- [5] W. Qiu, Y. Zhou, Z. Li et al., "Application of antibiotics/antimicrobial agents on dental caries," *BioMed Research International*, vol. 2020, Article ID 5658212, 11 pages, 2020.
- [6] N. Kulkarni and U. Muddapur, "Biosynthesis of metal nanoparticles: a review," *Journal of Nanotechnology*, vol. 2014, Article ID 510246, 8 pages, 2014.
- [7] L. Wang, C. Hu, and L. Shao, "The antimicrobial activity of nanoparticles: present situation and prospects for the future," *International Journal of Nanomedicine*, vol. 12, pp. 1227–1249, 2017.
- [8] K. S. Kavitha, S. Baker, D. Rakshith et al., "Plants as green source towards synthesis of nanoparticles," *International Research Journal of Biological Sciences*, vol. 2, pp. 66–76, 2016.
- [9] A. E. Albalawi, S. Abdel-Shafy, A. Khudair Khalaf et al., "Therapeutic potential of green synthesized copper nanoparticles alone or combined with meglumine antimoniote (glucantime®) in cutaneous leishmaniasis," *Nanomaterials*, vol. 11, no. 4, p. 891, 2021.
- [10] U. Kamran, H. N. Bhatti, M. Iqbal, and A. Nazir, "Green synthesis of metal nanoparticles and their applications in different fields: a review," *Zeitschrift für Physikalische Chemie*, vol. 233, no. 9, pp. 1325–1349, 2019.
- [11] G. Geoprincy, B. V. Srri, U. Poonguzhali, N. N. Gandhi, and S. Renganathan, "A review on green synthesis of silver nanoparticles," *Asian Journal of Pharmaceutical and Clinical Research*, vol. 6, no. 1, pp. 8–12, 2013.
- [12] S. K. Srikanth, D. D. Giri, D. B. Pal, P. K. Mishra, and S. N. Upadhyay, "Green synthesis of silver nanoparticles: a review," *Green and Sustainable Chemistry*, vol. 6, no. 1, pp. 34–56, 2016.
- [13] X. Li, L. Qu, Y. Dong et al., "A review of recent research progress on the *Astragalus* genus," *Molecules*, vol. 19, no. 11, pp. 18850–18880, 2014.
- [14] M. H. Shahrajabian, W. Sun, and Q. Cheng, "A review of *Astragalus* species as foodstuffs, dietary supplements, a traditional Chinese medicine and a part of modern pharmaceutical science," *Applied Ecology and Environmental Research*, vol. 17, no. 6, pp. 13371–13382, 2019.
- [15] J. L. Rios and P. G. Waterman, "A review of the pharmacology and toxicology of *Astragalus*," *Phytotherapy Research*, vol. 11, no. 6, pp. 411–418, 1997.
- [16] G. M. Sulaiman, W. H. Mohammed, T. R. Marzoog, A. A. al-Amiery, A. A. Kadhum, and A. B. Mohamad, "Green synthesis, antimicrobial and cytotoxic effects of silver nanoparticles using *Eucalyptus chapmaniana* leaves extract," *Asian Pacific Journal of Tropical Biomedicine*, vol. 3, no. 1, pp. 58–63, 2013.
- [17] N. P. Panpaliya, P. T. Dahake, Y. J. Kale et al., "In vitro evaluation of antimicrobial property of silver nanoparticles and chlorhexidine against five different oral pathogenic bacteria," *The Saudi Dental Journal*, vol. 31, no. 1, pp. 76–83, 2019.
- [18] CLSI, *Performance Standards for Antimicrobial Susceptibility Testing; Twenty-Second Informational Supplement*, The Clinical and Laboratory Standards Institute, Wayne, PA, 2012.
- [19] H. Xu, F. Qu, H. Xu et al., "Role of reactive oxygen species in the antibacterial mechanism of silver nanoparticles on *Escherichia coli* O157: H7," *Biomaterials*, vol. 25, no. 1, pp. 45–53, 2012.
- [20] M. A. El-Nakeeb, H. M. Abou-Shleib, A. M. Khalil, H. G. Omar, and O. M. El-Halfawy, "Membrane permeability alteration of some bacterial clinical isolates by selected antihistaminics," *Brazilian Journal of Microbiology*, vol. 42, no. 3, pp. 992–1000, 2011.
- [21] W. Du, C. Sun, Z. Liang, Y. Han, and J. Yu, "Antibacterial activity of hypocrellin A against *Staphylococcus aureus*," *World Journal of Microbiology and Biotechnology*, vol. 28, no. 11, pp. 3151–3157, 2012.
- [22] M. M. Bradford, "A rapid and sensitive method for the quantitation of microgram quantities of protein utilizing the principle of protein-dye binding," *Analytical Biochemistry*, vol. 72, no. 1–2, pp. 248–254, 1976.

- [23] T. Suwan, S. Khongkhunthian, and S. Okonogi, "Green synthesis and inhibitory effects against oral pathogens of silver nanoparticles mediated by rice extracts," *Drug Discoveries & Therapeutics*, vol. 12, no. 4, pp. 189–196, 2018.
- [24] A. E. Albalawi, "Antileishmanial activity of Ziziphus spinachristi leaves extract and its possible cellular mechanisms," *Microorganisms*, vol. 9, no. 10, 2021.
- [25] A. E. Albalawi, A. K. Khalaf, M. S. Alyousif et al., "Fe₃O₄@pir-octone olamine magnetic nanoparticles: Synthesize and therapeutic potential in cutaneous leishmaniasis," *Biomedicine & Pharmacotherapy*, vol. 139, no. 139, 2021.
- [26] H. Agarwal, S. V. Kumar, and S. Rajeshkumar, "A review on green synthesis of zinc oxide nanoparticles - An eco-friendly approach," *Resource-Efficient Technologies*, vol. 3, no. 4, pp. 406–413, 2017.
- [27] S. Jadoun, R. Arif, N. K. Jangid, and R. K. Meena, "Green synthesis of nanoparticles using plant extracts: a review," *Environmental Chemistry Letters*, vol. 19, no. 1, pp. 355–374, 2021.
- [28] T. M. Abdelghany, A. M. H. al-Rajhi, M. A. al Abboud et al., "Recent advances in green synthesis of silver nanoparticles and their applications: about future Directions. A Review," *BioNanoScience*, vol. 8, no. 1, pp. 5–16, 2018.
- [29] S. Emrani, R. Zhiani, and M. DafeJafari, "The biosynthesis of silver nanoparticles using plants of Glycyrrhiza glabra and Mentha Piperata and its antimicrobial effect on some bacterias that cause tooth decay," *Journal of Rafsanjan University of Medical Sciences*, vol. 16, no. 10, pp. 953–968, 2018.
- [30] S. Majeed and M. Khanday, "Green synthesis of silver nanoparticles using bark extract of Salix alba and its antimicrobial effect against bacteria isolated from dental plaque," *Oriental Journal of Chemistry*, vol. 32, no. 3, pp. 1611–1618, 2016.
- [31] A. E. Hernández-Gómora, E. Lara-Carrillo, J. B. Robles-Navarro et al., "Biosynthesis of silver nanoparticles on orthodontic elastomeric modules: evaluation of mechanical and antibacterial properties," *Molecules*, vol. 22, no. 9, 2017.
- [32] H. Tolouietabar and A. A. Hatamnia, "Investigation of antibacterial activity of silver nanoparticles synthesized from Scrophularia striata fruit extract," *Journal of Cell & Tissue*, vol. 8, no. 2, pp. 206–213, 2017.
- [33] K. S. Siddiqi, A. Husen, and R. A. Rao, "A review on biosynthesis of silver nanoparticles and their biocidal properties," *Journal of Nanobiotechnology*, vol. 16, no. 1, pp. 1–28, 2018.
- [34] Z. Yu, Q. Li, J. Wang et al., "Reactive oxygen species-related nanoparticle toxicity in the biomedical field," *Nanoscale Research Letters*, vol. 15, no. 1, pp. 1–4, 2020.
- [35] S. Rajesh, V. Dharanishanthi, and A. V. Kanna, "Antibacterial mechanism of biogenic silver nanoparticles of Lactobacillus acidophilus," *Journal of Experimental Nanoscience*, vol. 10, no. 15, pp. 1143–1152, 2015.
- [36] A. Abbaszadegan, Y. Ghahramani, A. Gholami et al., "The effect of charge at the surface of silver nanoparticles on antimicrobial activity against gram-positive and gram-negative bacteria: a preliminary study," *Journal of Nanomaterials*, vol. 2015, Article ID 720654, 8 pages, 2015.
- [37] S. Khorrami, A. Zarrabi, M. Khaleghi, M. Danaei, and M. R. Mozafari, "Selective cytotoxicity of green synthesized silver nanoparticles against the MCF-7 tumor cell line and their enhanced antioxidant and antimicrobial properties," *International Journal of Nanomedicine*, vol. 13, pp. 8013–8024, 2018.